JACS
JOURNAL OF THE AMERICAN CHEMICAL SOCIETY

pubs.acs.org/JACS

Article

Serial Femtosecond Crystallography Reveals that Photoactivation in a Fluorescent Protein Proceeds via the Hula Twist Mechanism

Alisia Fadini, Christopher D.M. Hutchison, Dmitry Morozov, Jeffrey Chang, Karim Maghlaoui, Samuel Perrett, Fangjia Luo, Jeslyn C.X. Kho, Matthew G. Romei, R. Marc L. Morgan, Christian M. Orr, Violeta Cordon-Preciado, Takaaki Fujiwara, Nipawan Nuemket, Takehiko Tosha, Rie Tanaka, Shigeki Owada, Kensuke Tono, So Iwata, Steven G. Boxer, Gerrit Groenhof, Eriko Nango,* and Jasper J. van Thor*

Cite This: *J. Am. Chem. Soc.* 2023, 145, 15796−15808

Read Online

ACCESS | Metrics & More | Article Recommendations | Supporting Information

ABSTRACT: Chromophore *cis/trans* photoisomerization is a fundamental process in chemistry and in the activation of many photosensitive proteins. A major task is understanding the effect of the protein environment on the efficiency and direction of this reaction compared to what is observed in the gas and solution phases. In this study, we set out to visualize the hula twist (HT) mechanism in a fluorescent protein, which is hypothesized to be the preferred mechanism in a spatially constrained binding pocket. We use a chlorine substituent to break the twofold symmetry of the embedded phenolic group of the chromophore and unambiguously identify the HT primary photoproduct. Through serial femtosecond crystallography, we then track the photoreaction from femtoseconds to the microsecond regime. We observe signals for the photoisomerization of the chromophore as early as 300 fs, obtaining the first experimental structural evidence of the HT mechanism in a protein on its femtosecond-to-picosecond timescale. We are then able to follow how chromophore isomerization and twisting lead to secondary structure rearrangements of the protein β-barrel across the time window of our measurements.

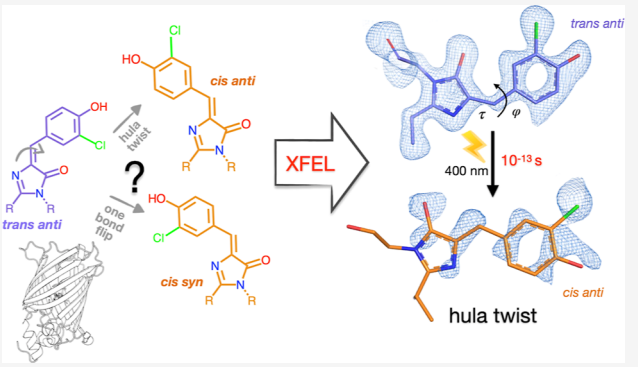

INTRODUCTION

The light-induced *cis/trans* isomerization of a chromophore double bond is a key reaction in photochemistry. In the dynamical response that follows photon absorption, photoisomerization has been shown to be the primary event for a variety of photoreceptors, such as visual pigments, and for the toolbox of photoactivatable proteins used for super-resolution microscopy.[1−4] A detailed understanding of the reaction pathway and of how it is steered by the protein environment is key for the rational design of more effective photosystems to employ in nanoscopy,[5−8] optogenetics,[2,9−13] and fluorescence biosensing.[14,15]

Despite the ubiquity of this reaction, the precise mechanism of photoisomerization in conjugated systems is hard to determine. Two conceivable pathways that a protein chromophore can follow for *cis/trans* photoisomerization are the one bond flip (OBF) and the hula twist (HT).[16] In the conventional OBF, the only bond to rotate is the one undergoing isomerization (τ in Figure 1—top);[17] half of the molecule needs to turn over, indicating that the OBF mechanism is expected to require a considerable amount of space to be available. In the 1980s, Liu and Asato reasoned that, in proteins, this volume-demanding transition seemed to be in contrast with the observed picosecond formation of an isomerized photoproduct: significant chromophore pocket residue rearrangements that might accompany a large volume sweep by the chromophore are unlikely to occur within such a timescale. As a volume-conserving alternative to the OBF for isomerization in bathorhodopsin, they proposed the HT mechanism, where both τ and the neighboring bond ϕ rotate simultaneously[18] (Figure 1—bottom). Since it has become generally accepted that photoisomerization in rhodopsins occurs through a bicycle-pedal mechanism, in which the *cis* conformation is propagated along the chromophore by a concerted rotation about parallel pairs of double bonds and not through a HT.[19−21] A recent time-resolved crystallographic study has in fact obtained structural evidence for an aborted

Received: March 3, 2023
Published: July 7, 2023

https://doi.org/10.1021/jacs.3c02313
J. Am. Chem. Soc. 2023, 145, 15796−15808

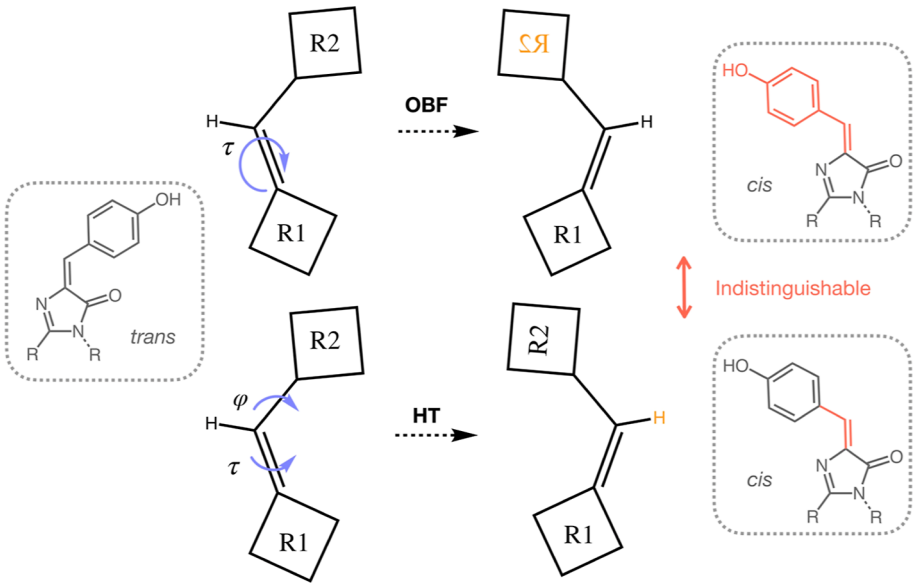

Figure 1. Schematic of potential chromophore photoisomerization pathways. Two possible pathways for the *cis/trans* photoisomerization of a chromophore are the OBF pathway or the HT pathway, both shown here schematically. The OBF mechanism involves the rotation of only the isomerizing bond, τ, and is expected to sweep a large volume, as half of the molecule is flipped in the process. In the HT pathway, on the other hand, both τ and its neighboring bond ϕ rotate simultaneously. The products formed by these two pathways are indistinguishable if the part of the molecule that flips is symmetric.

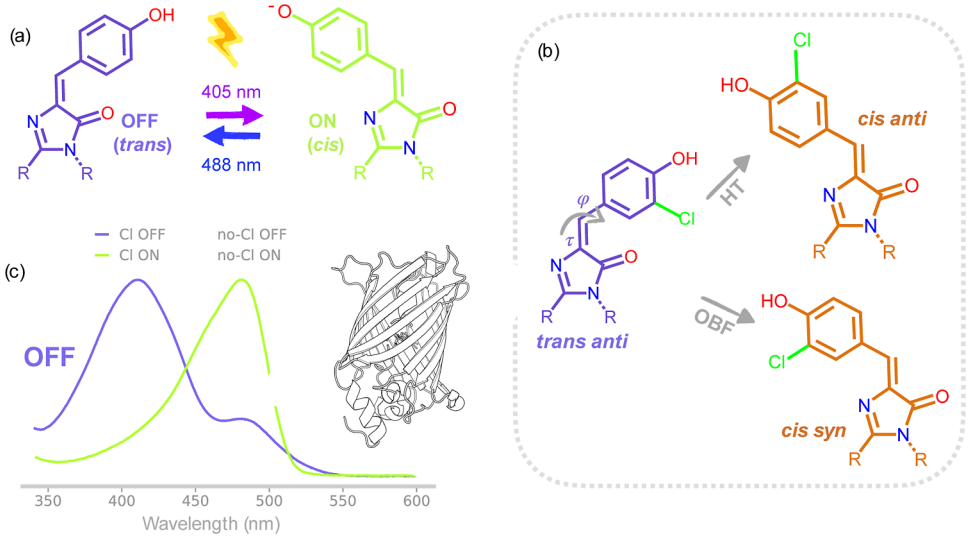

Figure 2. Cl-rsEGFP2 photoswitching. (a) Reversibly photoswitchable protein rsEGFP2 can be converted between a dark OFF state to a fluorescent ON state by specific frequencies of light. These changes are caused by a *trans*-to-*cis* isomerization and subsequent deprotonation of its embedded chromophore. (b) Addition of a chlorine substituent to the phenolate ring of the chromophore can break its C2 point group symmetry and allow us to distinguish between the HT and OBF mechanisms of chromophore photoisomerization in the first photoproduct of the OFF-to-ON reaction. The normalized absorption spectrum and structure of Cl-rsEGFP2 (c) possess very similar properties as the non-chlorinated protein: the OFF state absorbing predominantly at 400 nm and the ON state at around 480 nm, while the protein tertiary structure exhibits the β-barrel fold typical of GFP-like constructs. A 2 nm shift can be observed in the absorption profile between chlorinated and non-chlorinated constructs caused by the electron-withdrawing nature of chlorine.[47]

bicycle-pedal mechanism in a bovine rhodopsin starting at 1 ps.[22,23] Nonetheless, crystallographic data supporting the presence of two volume-conserving isomerization pathways, including the HT, were obtained for nanosecond intermediates of the photoactive yellow protein (PYP) photocycle.[24]

Conclusive experimental evidence or consensus for whether GFP-like chromophores that are functionally embedded in proteins undergo OBF or HT as the primary photoactivation pathway has not yet been obtained.[16,25−32] Two reasons for this are, first, that the primary photoproducts are formed on the ultrafast timescale and are very short-lived, requiring picosecond, or preferably femtosecond, time resolution to be distinguished. Second, the ground-state species formed immediately after photoisomerization by OBF and HT are indistinguishable if the part of the molecule that flips is symmetric (Figure 1). In this work, we address both these issues to determine the photoisomerization pathway in a

https://doi.org/10.1021/jacs.3c02313
J. Am. Chem. Soc. 2023, 145, 15796−15808

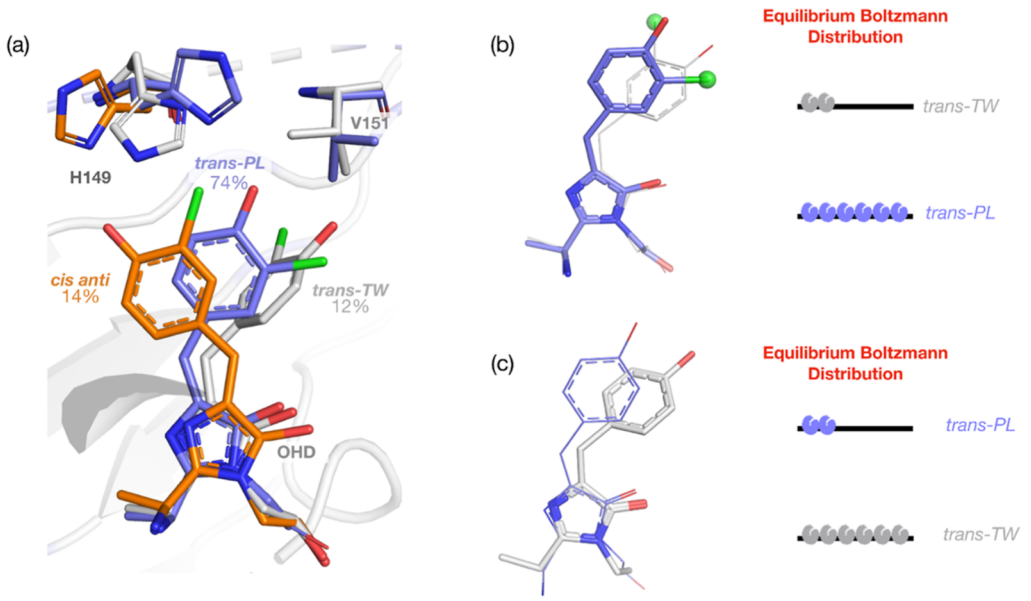

Figure 3. OFF-state chromophore configurations in Cl-rsEGFP2. (a) Refined Cl-rsEGFP2 dark OFF-state structure obtained from room-temperature serial femtosecond crystallography (PDB 8A6G). The predominant chromophore (OHD) conformation is the "planar" *trans anti* (*trans-PL*). Minor populations of a "twisted" *trans syn* (*trans-TW*) and of *cis anti* configurations are also modeled (refined occupancies of 12 and 14%, respectively). The three chromophore configurations are accompanied by three alternate His149 conformations. Two Val151 conformations are also resolved and matched to the *trans-PL* and *trans-TW* species. (b) OFF-state equilibrium *trans* structures of Cl-rsEGFP2 and (c) rsEGFP2.[44] The major configuration found in the OFF-state chlorinated structure is *trans-PL*, while it is *trans-TW* when the chlorine substituent is not present. We presume that the heavy atom substitution results in a higher energy for the *trans-TW* state through increased steric hindrance. See also Figures S4−S6, Table S3, and Note S1.

construct of the reversibly switchable fluorescent protein rsEGFP2.[33]

Reversibly switchable fluorescent proteins (RSFPs), such as rsEGFP2, can typically be converted between a fluorescent ON state and a non-fluorescent OFF state using specific photon wavelengths.[34,35] They have been widely employed in super-resolution microscopy and imaging;[36−42] rsEGFP2 in particular is a β-barrel protein that can be switched from its equilibrium ON state to the non-fluorescent state by 488 nm light, whereas the OFF-to-ON transition is achieved by illumination at 405 nm. In the fluorescent ON state, the chromophore is found as the anionic *cis* isomer, while the neutral *trans* isomer is responsible for the non-fluorescent OFF state (Figure 2a).[33,43] Time-resolved structural and spectroscopic data previously obtained for the OFF-to-ON reaction of rsEGFP2[44,45] identified the formation of a twisted chromophore intermediate within a couple of picoseconds and the presence of a ground-state protonated *cis* conformer 10 ns after photoexcitation, attributing deprotonation to a later, ground-state process. An experimental structural insight on the fundamental isomerization pathway and on the involvement of the speculated chromophore HT, however, remains lacking. As with previous studies, we focus here on the OFF-to-ON reaction, which has a higher quantum yield than the ON-to-OFF reaction.[43,46] The 4-hydroxybenzylidene-1,2-dimethylimidazolinone chromophore's phenol ring in rsEGFP2 has a C_2 point group symmetry, leading to equivalent *cis* products regardless of the photoisomerization pathway. We exploit the introduction of a chlorine atom substituent[47] to break this symmetry and distinguish between the products formed via the OBF and HT pathways, as previously suggested.[48] On the basis of IUPAC recommendations,[49−51] starting from a *trans* chromophore with a substituent *anti* to the double-bonded imidazolinone nitrogen, HT leads to a *cis anti* product, while the configuration formed via OBF is *cis syn* (Figure 2b). The motivation behind incorporation of chlorine in rsEGFP2 is therefore to obtain a construct with photoswitching capabilities that resemble those of rsEGFP2[48] but that can be investigated to confirm either HT or OBF. We note below that there are structural and spectroscopic differences between the chlorinated and unmodified constructs and the observation of the HT pathway in the chlorinated construct we consider here does necessarily imply such process in other constructs.

In a prior study,[48] the same rsEGFP2 construct containing a monochlorinated chromophore (Cl-rsEGFP2) was used to study the ON-to-OFF reaction and compare protein structures before and after irradiation. Structures were obtained by rapidly cryocooling crystals after a specific irradiation period and subsequently collecting diffraction data using synchrotron X-ray radiation. This method relied on the assumption that the cryocooled irradiated structure reflected the chromophore configuration immediately after photoisomerization but was not able to account for thermal bond rotations, which can interconvert *anti* and *syn* species, or any change in chromophore configuration induced by the freezing process itself. Here, by performing a time-resolved serial femtosecond crystallography (TR-SFX) experiment with sub-picosecond resolution, we have been able to unequivocally identify the primary photoproduct of the OFF-to-ON photoisomerization reaction: the *trans anti* chromophore in the OFF state of Cl-rsEGFP2 is photoexcited with a 400 nm photon, and clear signals showing the formation of a *cis anti* photoproduct are reported starting at delays of 300 fs. This, to our knowledge, is the first direct experimental structural evidence that unequivocally supports HT chromophore photoisomerization in a protein on its ultrafast timescale, more than 30 years after it was first hypothesized.

https://doi.org/10.1021/jacs.3c02313
J. Am. Chem. Soc. 2023, 145, 15796−15808

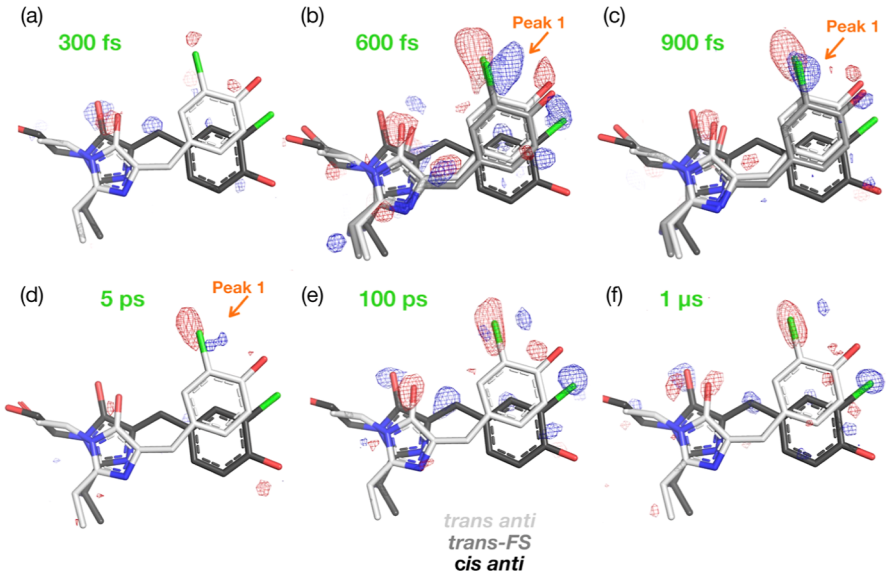

Figure 4. Time-resolved DED maps of Cl-rsEGFP2. Q-weighted DED maps for the collected pump−probe delays. Positive (blue) and negative (red) DED is shown at ±3.5 σ. The refined *trans anti* and *cis anti* species are shown in light and dark gray, respectively. In the 600 fs, 900 fs, and 5 ps maps, the feature "Peak 1" is highlighted: this is the main indicator of the presence of a femtosecond intermediate, which we have called *trans-FS* and discussed with further details in the main text. PDBs (in order) 8A6N, 8A6O, 8A6P, 8A6Q, 8A6R, and 8A6S. See also Figures S7−S13.

RESULTS AND DISCUSSION

OFF-State SFX Structure for Cl-rsEGFP2. Cl-rsEGFP2 maintains very similar switching properties to rsEGFP2 (Figures 2c and S1) and is expressed using amber suppression as described by Chang et al.[48] Cl-rsEGFP2 microcrystals diffracted to 1.63 Å at the SACLA X-ray Free Electron Laser (XFEL) in Japan (Figure S2). Crystals were pre-illuminated with a 488 nm CW laser in order to photoaccumulate the OFF state. The OFF-to-ON transition was then initiated with a 75 fs 400 nm pump laser pulse and probed with the XFEL pulse at pump−probe delays between 300 fs and 1 μs. To obtain a ground-state room-temperature structure of the Cl-rsEGFP2 OFF state, dark data was collected in an interleaved manner (1:5 ratio) with the pump−probe data throughout our TR-SFX experiment. To account for pump laser scatter during sample delivery and to model a more accurate dark structure, a dataset was also collected with a negative pump delay (−5 ps). A dark structure (PDB 8A6G) was refined to the interleaved dark dataset (Figure 3a) and confirmed through 2mFo-DFc and mFo-DFc maps obtained with the −5 ps data (Figure S4). This presents the chromophore primarily in a planar *trans anti* configuration (named here *trans-PL*). Minor populations of a twisted *trans syn* (named *trans-TW*) and of a *cis anti* species were also manually refined to occupancies of 12 and 14%, respectively, as well as the accompanying alternate conformations of residues H149 and V151 (Figures 3 and S4). The *trans-PL* and *trans-TW* species we observe here have been previously reported in room-temperature crystal structures of rsEGFP2[44,52] and in cryostructures of Cl-rsEGFP2[48] (Table S3). Absorption spectra and quantum chemical calculations also point to the presence of these two forms in rsEGFP2 solutions.[52] We expect that the ON-to-OFF reaction starting from the *cis* chromophore can therefore eventually result in either of these two *trans* conformations.

Adam et al.[52] postulate a fast exchange between *trans-PL* and *trans-TW* in solution (on the order of ≈0.1 s) and propose that the two states are separated by a low energy barrier in the protein conformational energy landscape. In room-temperature rsEGFP2 SFX structures, the prevalent *trans* configuration is the twisted *trans-TW* (Figure S5 and ref 52), suggesting that it is a lower energy state than *trans-PL*. In Cl-rsEGFP2, we observe the prevalent configuration to be *trans-PL* and presume that the transition from the planar to the twisted form is no longer energetically favorable due to the steric hindrance introduced by the bulk of the chlorine atom or to an electronic substituent effect (see also Note S1). This is also in line with the finding that an enlargement of a chromophore pocket residue (V151L) can shift the OFF state equilibrium almost completely to *trans-PL* in non-chlorinated rsEGFP2.[52] The states observed in our dark OFF-state structure are shown in Figure 3b. For the scope of this time-resolved study, we expect that any observed photoinduced species result from the *trans-PL*-to-*cis* reaction; since the starting population of *trans-TW* in our dark-state structure is below 15%, we expect that any photoproduct resulting from photoexcitation of this state will not be detectable in our data.

TR-SFX Data for Cl-rsEGFP2. *Chromophore-Specific Changes.* Pump−probe TR-SFX data was collected for six delays: 300 fs, 600 fs, 900 fs, 5ps, 100 ps, and 1 μs. The pump laser power density used was 0.5 mJ/mm^2. We generated Q-weighted difference electron density (DED) maps for these delays and improved signal-to-noise through principal component analysis using a python pipeline (Figures S7 and S8 and Supporting Information Procedures Section 1). The resulting maps are shown in Figure 4 at ±3.5σ. The initial negative density signals on the *trans-PL* imidazolinone ring oxygen are already visible at 300 fs and are accompanied by respective positive density on the same oxygen and on the *cis* methylene bridge. At 600 fs, there is a large negative density on the *trans-PL* Cl atom, and negative signals also on the two chromophore oxygens and methylene bridge. Positive density signals appear on both *cis anti* rings. In the 600 and 900 fs data, there is also a strong (+5σ) positive feature that we have labeled Peak 1 and suggests an upward shift of chlorine position (approximately 1 Å—Figure 4b,c). This peak is still weakly present in the 5 ps data (Figure 4d) and effectively

https://doi.org/10.1021/jacs.3c02313
J. Am. Chem. Soc. 2023, 145, 15796−15808

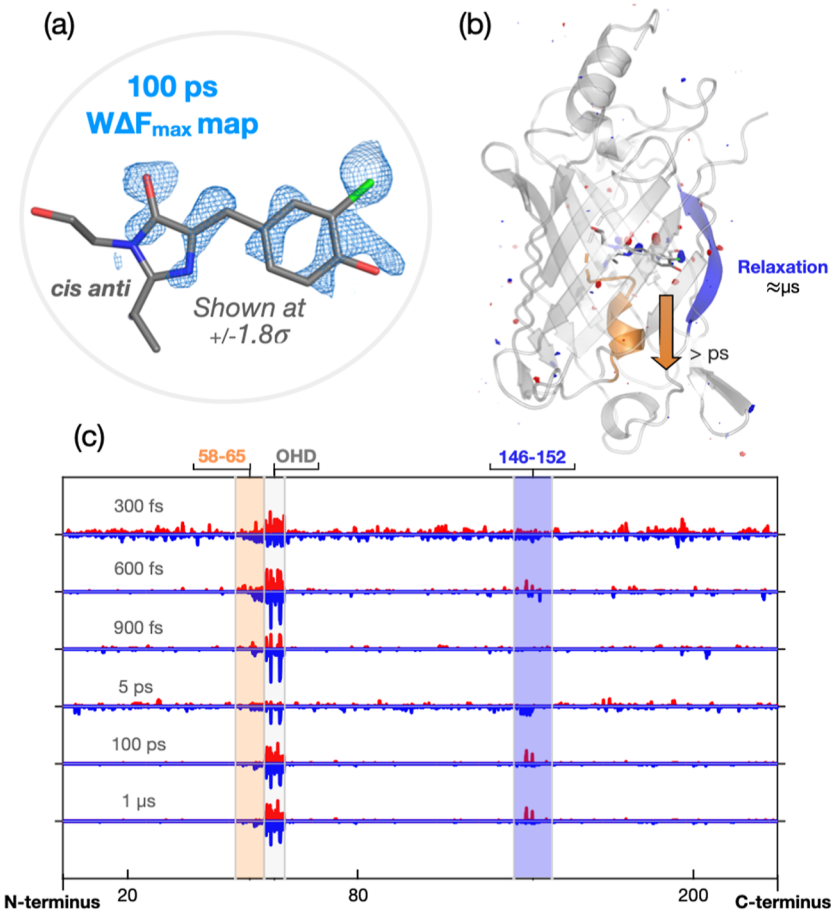

Figure 5. Light-induced changes across the entire Cl-rsEGFP2 protein structure. (a) The background-subtracted map ($W\Delta F_{max}$) for the 100 ps dataset clearly outlines the presence of the *cis anti* photoproduct. (b,c) The strongest signals in the *Q*-weighted DED maps for the collected time points are concentrated on the chromophore (OHD). However, by moving a spherical volume through all the atoms in the protein and integrating the negative and positive electron density within it, two other regions of variation stand out: the central α-helix (residues 58−67, orange) and the β-strand 7 (residues 146−152, blue). Signals in the α-helix are strongest in the early data points (c) and suggest a downward shift of the helix [(b) and Figure S15]. Negative density signals on β-strand 7 (Figure S16) are strongest on the late picosecond−microsecond timescale and suggest an increase in conformational flexibility for this secondary structure element. See also Figures S9−16.

absent in the 100 ps and 1 μs maps. We assign Peak 1 to an intermediate state, which we call *trans-FS* (Figure 4b), discussed in more detail below. At 100 ps and 1 μs, the *trans-PL* to *cis anti* features are very clear and are the prevalent signals at $\pm 3.5\sigma$: there are strong negative and positive features on the chromophore chlorine substituent and on the imidazolinone ring carbonyl, as well as positive density on the *cis anti* methylene bridge and the phenol ring (Figure 4e,f). These difference density signals thus point to increased population of the *cis anti* species and decreased population of *trans anti* starting from 300 fs, as well as possible formation of a femtosecond intermediate. In the analysis below, we investigate this further to refine the structure and occupancy of the *cis anti* and *trans-FS* conformations for each time point.

In TR-SFX, photoinduced differences in structure factor amplitudes, caused by population changes prepared by the pump laser pulse, are usually small. A further analysis is therefore implemented to extract these minor light-induced population changes from the structure factors obtained for each time point, once key regions of interest are identified from the DED maps above (e.g., the chromophore region). This method is based on the background subtraction estimation implemented by Pearce and colleagues[53] and consists of generating maps, called here $W\Delta F_{max}$ maps, from the measured illuminated and dark structure factors and reference phases. These maps differ from the DED maps above in that a background subtraction factor ($0 < N_{bg} < 1$) is estimated to generate a $w(|F_{illuminated}| - N_{bg} \times |F_{dark}|)$ weighted map (Figures S9−S12 and Supporting Information Procedures Section 1). The $W\Delta F_{max}$ map for the 100 ps time point is shown in Figure 5a and illustrates the efficacy of the background estimation: the *cis anti* photoproduct is clearly present, with electron density at $+1.8\sigma$ outlining both rings and a large portion of the isomerized double bond. $W\Delta F_{max}$ maps for 300 fs, 600 fs, 900 fs, and 1 μs also confirm the formation of the *cis anti* species (Figure S11). The 600 and 900 fs $W\Delta F_{max}$ maps support the assignment of Peak 1 to a *trans* intermediate. The electron densities of these two maps are very similar and present four key characteristics: (i) the presence of peak 1, (ii) an elongated and uncentered peak where the *cis anti* chlorine is positioned, which is in contrast with the round, centered features visible in the $W\Delta F_{max}$ maps from the later time points, (iii) electron density that fills the *cis anti* chromophore phenol ring, again in contrast with the 100 ps and 1 μs maps that show instead a clear outline of the chromophore phenol ring where its center is empty, and (iv) features that suggest a tilt of the imidazolinone ring oxygen toward the phenol ring (Figures S11 and 12). Though assignment is complicated by the likely

https://doi.org/10.1021/jacs.3c02313
J. Am. Chem. Soc. 2023, 145, 15796−15808

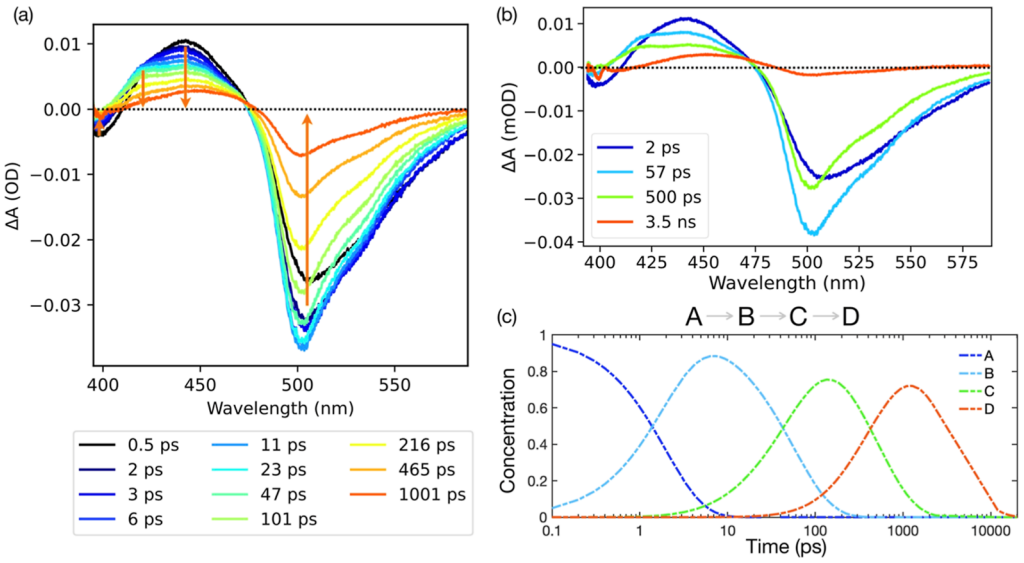

Figure 6. Femtosecond Cl-rsEGFP2 TA data. (a) Transient difference absorption spectra recorded at different pump−probe time delays after a femtosecond laser excitation (400 nm) starting from the Cl-rsEGFP2 OFF state. (b) Components fitted through global analysis of the data shown in (a). (c) Raw concentration profiles for the four components globally fitted using a sequential model. See also Figures S17 and S18.

presence on both *trans-FS* and *cis anti* species, refinement of coordinates to 600 and 900 fs $W\Delta F_{max}$ maps leads to two chromophore configurations that are almost superimposable (Figure S13). We therefore suggest that an intermediate state, *trans-FS*, accumulates with a 600−900 fs timescale. Because the 900 fs data appears to have less contamination from the *cis anti* species than the 600 fs data, we take the coordinates refined from the 900 fs $W\Delta F_{max}$ map as the proposed *trans-FS* structure. This chromophore configuration is still *trans* but more twisted (the torsion angles for the refined structure are $\phi \approx 33°$ and $\tau \approx 178°$); such change is accompanied by a movement of the imidazolinone ring by about 0.5 Å, which is particularly noticeable from the shift in the electron density of its oxygen (Figure 4). Comparable ultrafast formation of a twisted *trans* chromophore in protein photoisomerization has been observed before in rsEGFP2[45] and PYP[54] and has been assigned to the excited state. Similarly, we also suggest assignment of *trans-FS* to an excited-state species on the basis of QM-MM calculations (see below). $W\Delta F_{max}$ maps thus allow us to model photoinduced species more effectively than the DED maps in Figure 4. Through them, we confirm positioning of the *cis anti* configuration as well as the structure of the *trans-FS* intermediate (Figures 5 and S10−S13). After establishing coordinates through $W\Delta F_{max}$ maps, we use the raw data once again to refine occupancies of new chromophore conformations for each time point (Figure S14). We note that clear identification of photoproduct and intermediate species here is greatly helped by the higher X-ray scattering cross-section of chlorine, both in DED and in $W\Delta F_{max}$ maps, highlighting a further advantage of introducing a heavy atom substituent in the chromophore structure. The confident assignment of *cis anti* formation at ultrafast time points provides strong evidence for the HT pathway in this rsEGFP2 construct. The observation of photoisomerization at femtosecond delays is likely associated with the relatively high primary quantum yield of this protein. The significant transient concentration and large displacement of the chromophore in the reactive pathway of Cl-rsEGFP2 strongly contribute to the light-induced differences, while additional contributions, such as vibrational coherences, will be below this level.

Protein Residue/Structure Changes. Strong DED features in our data are almost entirely concentrated on the chromophore (Figure 5b). To investigate the presence of any other motions across the protein structure that are associated with chromophore twisting and photoisomerization, we use the analysis and scripts from Wickstrand et al.[55] and plot DED signals along the protein sequence for every time point collected (Figure 5c). Data from 600 fs, 900 fs, 100 ps, and 1 μs delays display the best crystallographic statistics (Table S1), so we concentrate on these to identify the areas of further protein structural change. Aside from the chromophore (the OHD ligand in the structures) that, as expected, presents the largest light-induced differences, there are two regions of notice: the central α-helix (residues 58−67) and β-strand 7 (residues 146−152), which interfaces with the chromophore phenol ring. Figures S15 and 16 show the DED on specific residues of these two secondary structure elements for different time points. Signals on the central α-helix suggest an overall downward motion of the region by around 1.4 Å if the distance between the strong positive/negative features on Leu65 and Thr63 is measured. A downward movement of this helix was previously observed in 1 ps DED maps of non-chlorinated rsEGFP2[45] and was attributed to a tilt of the imidazolinone ring upon chromophore twisting. Similarly, here the prevalence of these signals in the sub-picosecond time points indicates that this motion is closely associated with the ultrafast photoisomerization of the bound chromophore or formation of the twisted *trans-FS* intermediate.

Negative DED signals on the side chains and backbone of β-strand 7 (β7) residues Asn147, Asn150, and Val151 are superimposable between the 100 ps and 1 μs datasets and hint at increased structural flexibility of this secondary structure element at later time points. Conformational fluctuations involving mainly β7, as well as that side of the β-barrel (β7−10), have been reported on the nanosecond−millisecond timescale for multiple GFP-like proteins,[56−61] including rsEGFP2.[61] This structural relaxation and plasticity that arises

https://doi.org/10.1021/jacs.3c02313
J. Am. Chem. Soc. 2023, 145, 15796−15808

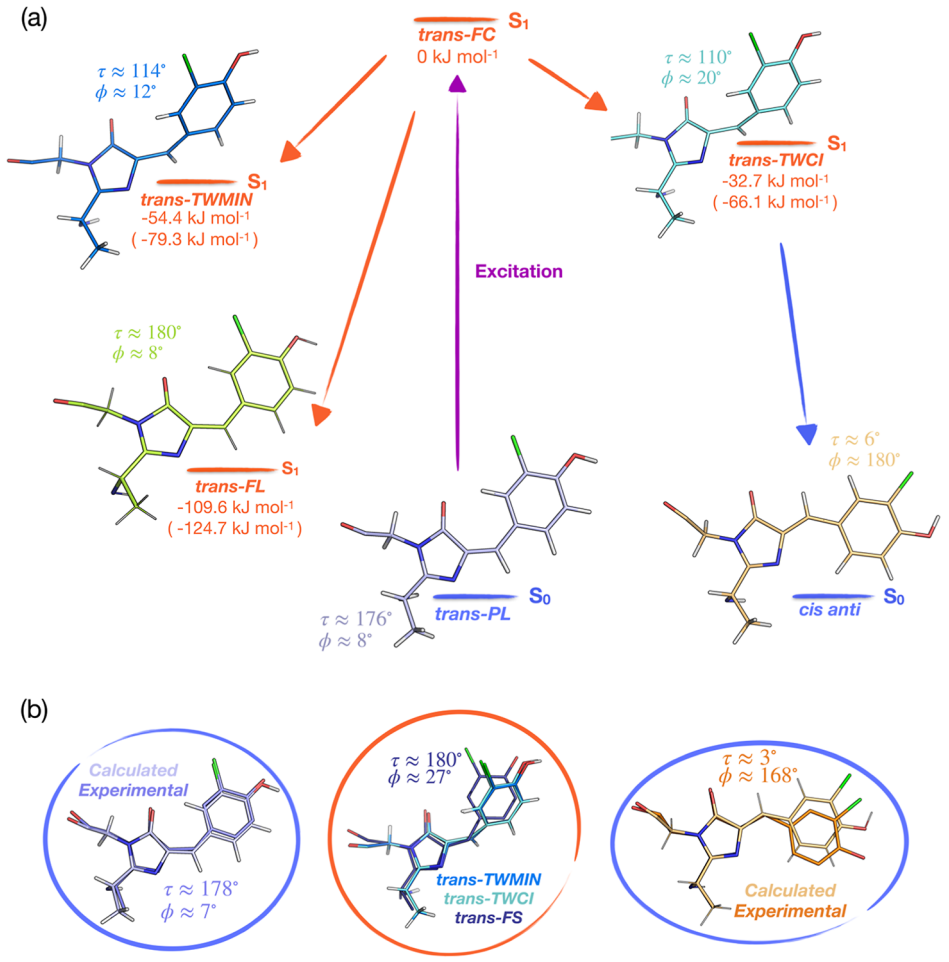

Figure 7. Comparison between experimental and calculated chromophore structures. (a) Molecular structures obtained through QM-MM modeling before and after CI crossing are shown with their energy arrangement relative to the Franck−Condon point and their respective torsion angles. Relative energy values computed at a lower (SA2-CASSCF(12,11)/3-21G//Amber03) and higher (XMCQDPT2/SA6-CASSCF(12,11)/cc-pVDZ//Amber03—in parenthesis) level of theory are stated (see also Section 4 in the Supporting Information Procedures). The photoexcited *trans-PL* species isomerizes in the protein binding pocket to the planar *cis anti* via HT, passing through a highly twisted conformation near the CI (*trans-TWCI*). An excited-state twisted minimum structure (*trans-TWMIN*) and a fluorescent *trans* minimum (*trans-FL*) are also found. (b) The calculated conformations are compared to the planar *trans anti* and *cis anti* species, as well as to the twisted *trans-FS* intermediate, refined from TR-SFX data. See also Figure S19.

after photoactivation has been hypothesized to be important for efficient photoswitching between distinct protein conformations based on NMR, spectroscopy, and MD results.[57,59,60] We have now obtained time-resolved crystallographic evidence that supports the development of β7 dynamics starting from 100 ps and peaking in the microsecond regime (Figures 5 and S16) in Cl-rsEGFP2. In our maps, β7 motions are accompanied by a flip of His149 from its characteristic OFF conformation to its ON conformation[44,45,48] (Figure S16). The negative density on the side chain of His149 that indicates the flip to its ON conformation becomes clear at 1 μs, agreeing with recent time-resolved multiple-probe infrared spectroscopy (TRMPS-IR) data[61] that assign His149 movement to a 42 ns time constant following ultrafast chromophore photoisomerization.

Ultrafast Visible Transient Absorption Spectroscopy of Cl-rsEGFP2 Solutions. We monitored the spectral changes induced by 400 nm laser excitation in solutions of Cl-rsEGFP2 in the OFF state (Figure 6a). The first photoinduced spectral changes we observe include an increase in absorption at 450 nm that peaks at around 500 fs (attributed to excited-state absorption—ESA), accompanied by ground-state bleach (GSB) in the 400 nm region and a broad stimulated emission (SE) signal around 530−540 nm. Global analysis groups these features in a first component that has a decay rate constant of 2 ps. Assuming a sequential model (see Experimental Methods Section), this first component decays into a second and then a third component that both present a new positive peak at 420 nm and respective decay rate constants of 57 and 500 ps. In the final 3.5 ns component, the absorption at 420 nm is absent, and the main positive peak present is once again at 450−460 nm (Figure 6b,c). While the wavelengths for GSB, 450 nm ESA, and SE present in Cl-rsEGFP2 time-resolved spectra closely match those of rsEGFP2 (Figures S17 and 18 and refs 44 and 61), the transient picosecond positive peak at 420 nm is unique to the chlorinated construct (Figure S18). We also note that Cl-rsEGFP2 presents an interesting property of the stimulated emission band, which actually increases on the 2 ps timescale and then begins its decay with a 57 ps time constant. Such behavior is not observed in rsEGFP2 (Figures S17 and 18 and refs 44 and 61). We discuss this and the 420 nm positive feature in the following sections.

https://doi.org/10.1021/jacs.3c02313
J. Am. Chem. Soc. 2023, 145, 15796−15808

Quantum Chemical Analysis of HT Photoisomerization. To provide additional support for a HT photoisomerization pathway, we performed QM/MM optimizations at the SA2-CASSCF(12,11)/3-21G//Amber03 level of theory, in which we searched for conical intersections (CIs) associated with the OBF and HT isomerization mechanisms.[62] At first, we optimized a planar *trans* S_1 fluorescent minimum structure (*trans-FL*, Figure 7), which is further discussed below. Whereas no CI could be located along the OBF pathway, we could identify a minimum energy conical intersection (MECI) for a HT isomerization. Additionally, we performed re-computation of the energies in the optimized structures at the correlated XMCQDPT2/SA6-CASSCF(12,11)/cc-pVDZ//Amber03 level of theory. For a detailed description of these calculations, see the Supporting Information Procedure Section 4. It should be noted that the MECI is not a stationary point on the molecular potential energy surface but rather a geometry through which radiationless deactivation from the electronic excited to ground state occurs with high probability. The geometry at this CI features a ϕ torsion angle of 20° and a τ torsion angle of 110° (Figure 7b, *trans-TWCI*). Geometry optimizations in the electronic ground state confirm that this CI connects the neutral *trans* and *cis* chromophore conformers (Supporting Information Procedures Section 4). The value of τ in this *trans-TWCI* species is close to orthogonality and could suggest a stepwise (rather than concerted) nature to the HT pathway, though this additional detail is not resolved in our crystallographic data. At the levels of theory employed here, the *trans-TWCI* geometry is lower in energy than the Franck–Condon point (Figure 7a). Thus, the results of our computations suggest that the HT dominates the isomerization process, while the OBF mechanism is suppressed.

In addition to the HT MECI geometry (*trans-TWCI*), we also identified a twisted S_1 minimum geometry, with a ϕ torsion angle of 12° and a τ torsion angle of 114° (Figure 7b, *trans-TWMIN*), in line with the results from previous computations on the non-chlorinated HBI chromophore.[63,64] This resembles the *trans-FS* structure refined from the 600–900 fs datasets. Because the energy required for photon absorption from this minimum into the S_5 state is 434 nm and hence close to the transient absorption (TA) peak at 420 nm in the time-resolved TA spectroscopy measurements (Figure 6), the twisted S_1 minimum could tentatively be assigned to the transient intermediate responsible for this absorption. A more confident assignment, however, would require TA measurements on crystalline samples to determine if the kinetics of the 420 nm absorption confirm accumulation of the *trans-FS* species in 600–900 fs.

CONCLUSIONS

This study exemplifies the capability of the temporal and structural resolution available with serial crystallography at XFEL facilities. Through the combination of the SFX technique and the breaking of the rsEGFP2 chromophore symmetry via a heavy atom substituent, we resolve the primary photoproduct of the *trans*-to-*cis* photoisomerization and confidently assign it to be the outcome of a HT pathway. To our knowledge, this is the first experimental observation of HT photoisomerization in a protein on the femtosecond-to-picosecond timescale.

We additionally identify a twisted intermediate state at 600–900 fs that can potentially be assigned to an excited-state minimum on the basis of calculations. While we observe a possible correspondence between the calculated absorption spectrum of this intermediate and the 420 nm feature in our time-resolved TA spectra, we note that the sub-picosecond DED signal is dominated by the strongest displacement and highest ordering, and this may contribute only to the first decay component of the ESA and SE heterogeneous decay kinetics. The structural data obtained from TR-SFX reports on the thermodynamic distribution, displacements, cross-sections, and concentrations of ground and excited states in the protein at a specific point in time, while TA data is a kinetic description of the often heterogeneous electronic dynamics that depend on the spectroscopic selection rules. Because of this, the signal strengths and kinetics of TR-SFX and TA transients are not necessarily expected to be the same. In this case, we believe that further investigation, such as a pump–dump scheme, would be required for a confident connection between the crystallographic and spectroscopic signals we report. The current experimental evidence does not unequivocally support the involvement of the twisted *trans-FS* minimum in the reaction mechanism. In fact, given the observed sub-picosecond formation of the *cis anti* photoproduct, the presence of a twisted structure with a picosecond lifetime, and the predicted planar *trans*-S_1 fluorescent minimum from calculation (*trans-FL* in Figure 7), we speculate that there are (at least) three major decay channels in Cl-rsEGFP2: (i) an ultrafast, energetically down-hill access to the MECI to form the HT photoproduct, (ii) relaxation into the *trans-FL* minimum, and (iii) twisted *trans* S_1 minimum formation (*trans-FS*/*trans-TWMIN*). The last two cases can both promote fluorescence by transiently trapping the excited-state population and could provide an explanation for the long-lived fluorescent state observed in solution TA spectroscopy data (Figure 6).

The ability to track atomic displacements immediately following photon absorption is shown here to be essential for resolving the reaction pathway without having to rely on assumptions on the timescales of thermal bond rotations that can occur after photoactivation. The calculations presented and the use of room-temperature SFX suggest, in fact, that the HT is the only accessible photoisomerization coordinate in the Cl-rsEGFP2 chromophore pocket and that previously proposed crystal-packing constraints are most likely artifacts resulting from the cryo-trapping procedures used (Note S1 and ref 48). Our results thus support the reasoning that the protein cage in Cl-rsEGFP2 hinders the OBF mechanism in favor of the HT.

What is the significance of this pathway? The presence of *cis anti* photoproduct signals as early as 300 fs introduces the possibility of this photoisomerization reaction being a vibrationally coherent process, as observed for rhodopsins.[65−69] Vibrational dephasing times in GFP proteins have typically been reported to be within 1–2 ps,[70−72] which does not exclude the 300 fs *cis anti* species to be the product of a vibrationally coherent photoisomerization. Further work, such as coherently controlling the photoisomerization and tracking its yield,[67] would be required to investigate this. Interestingly, Adam and colleagues report that rsEGFP2 mutants in which the available binding pocket volume is decreased switch to their ON state much more efficiently than mutants where the available binding pocket volume is increased.[52] It will be valuable to investigate whether a HT reaction pathway dictated by a volume-constraining protein cage is responsible for this increased switching capability and whether coherent CI

https://doi.org/10.1021/jacs.3c02313
J. Am. Chem. Soc. 2023, 145, 15796−15808

crossing is important for the efficiency of photoactivation. Understanding the details of the photoactivation process such as these holds significant promise for the rational engineering of fluorescent proteins like Cl-rsEGFP2.[14,15,73−75] Serial femtosecond crystallography has also allowed us here to trace the effects of the early photoisomerization event to secondary structure rearrangements that occur later in time. This data provides time-stamped structural insight that integrates and reconciles previous observations from other experimental and computational techniques; it furthers our understanding of the dynamics that enable protein function through photoactivation and develops our ability to intelligently manipulate them for improved performance.

EXPERIMENTAL METHODS

2021 SFX Sample Preparation, Data Collection, and Setup. *Protein Expression, Purification, and Crystallization.* Recombinant expression was performed in BL21 (DE3) cells with a pET-15b vector for the rsEGFP2 gene and a pUltra vector containing the 3-chlorotyrosine amber suppression codon. The latter vector was used instead of the pEVOL vector described by Chang et al.[48] Large-scale bioreactor fermentation proceeded with a 50 L culture in Terrific Broth Modified (46.7 g/L) containing 100 mg/L ampicillin, 50 mg/L spectinomycin, 10.1 g/L glycerol, and 0.1 g/L 3-chlorotyrosine at 37 °C. After reaching an OD_{600} nm of ≈2, the culture was cooled to 20 °C, and induction was carried out by the addition of 0.24 g/L isopropyl β-D-1-thiogalactopyranoside. The culture was grown overnight for 17 h, harvested by pelleting, and stored at −20 °C.

Thawed cell pellets were washed with 50 mM Tris−HCl pH 8.0, 100 mM NaCl, 0.1 mg/mL DNase I, and 1 tablet of EDTA-free protease inhibitors per 100 mL of cells. Lysis was carried out at 4 °C with two passes at 35 kpsi in a T5 Cell disruptor (Constant Systems, UK). The lysate was centrifuged at 142 000 × *g* and 4 °C for 30 min before incubating the cell free extract with Ni-NTA resin for 45 min while shaking. After loading the slurry onto a glass column, the bound protein was washed with 2 column volumes of the above buffer containing 20 mM imidazole, followed by 2 column volumes containing 30 mM imidazole. The protein was then eluted with 200 mM imidazole, concentrated, and buffer-exchanged into 50 mM Hepes pH 7.5 and 100 mM NaCl using Vivaspin 10 kDa MWCO filters at 4 °C. The final purification step was carried out with a Superdex S75 gel filtration resin, and the main fractions were concentrated and finally buffer-exchanged into 50 mM Hepes pH 7.5 and 200 mM NaCl. The protein was either stored at −20 °C or used for crystallization.

Seeded batch crystallization proceeded with a final protein concentration of 20−24 mg/mL in a buffer consisting of 75 mM Hepes pH 8, 20 mM NaCl, and 1.1−1.3 M ammonium sulfate at 20 °C. Cuboid crystals with typical dimensions of 4−8 × 4−8 × 20−80 μm were obtained after 3 days.

Sample Preparation and Injection. Before injection, the crystals were buffer-exchanged into 25% PEG buffer and size-selected using a 50 μm filter and subsequently a 30 μm filter. Crystals were then delivered to the interaction region using a SACLA's droplet-on-demand injector (MICROJET)[76] and an 80 μm nozzle. Volumes of around 250 μl of crystal slurry were reverse-loaded through the jetting aperture to reduce the risk of blockages. The crystal slurry density was between 2 and 5 × 10^7 crystal/mL. The driving voltage for the injector piezo was normally 110 V, and current pulses were 100 μs long. Throughout the experiment, a hit rate between 30 and 60% was maintained.

SFX Data Collection and Optical Setup. 2021 data at SACLA[77] was collected at Experimental Hutch 2 of BL3. The detector used was the MPCCD-phase III detector,[78] and the detector distance was refined to 49.2 mm using unit cell distributions. The XFEL was operated with a repetition rate of 30 Hz, a photon energy of 10.5 keV, and a focal spot of ≈1.5 μm in full width at half-maximum (FWHM). Crystals were pre-illuminated by direct illumination of the glass tip of a droplet injector with an unfocused (≈2 mm beam size) 100 mW 488 nm CW laser. Offline testing with the same laser and crystal concentration demonstrated maximum conversion after 2 s of illumination well within the ≈8 s transit time of the illuminated part of the jet during normal operation. 400 nm optical pump pulses were created by second harmonic generation of the SACLA synchronized femtosecond laser system using a 100 μm BBO crystal. The pulse length of 800 nm fundamental was measured to be 75 fs by autocorrelation. 7.5 μJ pump pulses were focused onto the interaction region using a 300 mm lens to give a spot size of 130 μm (FWHM) and a corresponding energy density of 0.5 mJ/mm^2. Light and dark data were interleaved in a 5:1 ratio. A spatial overlap between the optical and XFEL beams was confirmed using a 50 μm Ce:YAG crystal. The same crystal was used to perform a cross-correlation and find a temporal overlap; the cross-correlation was fitted using the same methods described in 79. A temporal jitter between the optical and X-ray pulses was monitored using the SACLA timing tool system;[80] however, recent upgrades to the synchronization of the optical laser and XFEL[81] showed that the measured jitter measured was ≈50fs (FWHM) less than the instrument response of the measurement (≈100 fs), indicating that post-processing sorting of the TR-SFX data was unnecessary. The new system also actively corrects for slow timing drift between optical and XFEL beams, which was confirmed by cross-correlation measurements at the start and end of data collection (see SI for more details). Following data analysis methods are detailed in Section 1 of the Supporting Information Procedures.

Femtosecond TA Spectroscopy. Femtosecond TA data was measured using the system described in Lincoln et al[82] White light probe pulses were generated using filamentation in a CaF_2 glass window. 400 nm pump pulses were generated by doubling the fundamental 800 nm (Hurricane, Spectra Physics) in a 100 μm-thick SHG-BBO (Eksma optics). The pump pulses were focused onto the sample using an AR-coated f = 500 nm lens (Thorlabs). The pump energy density was ≈0.02 mJ/mm^2. A 20 μl solution of Cl-rsEGFP2 was mounted in a liquid flow cell (Harrick Scientific Products Inc) between a 1 mm (front) and a 2 mm (back) sapphire windows (Crystran Ltd) using a 25.6 μm spacer. The sample concentration was chosen to give an OD of ≈0.1 at the 400 nm peak of the OFF state (Figure 2c). The sample was pre-illuminated using an unfocused 50 mW 488 nm diode laser to ensure presence of the target OFF state and was continuously translated during data collection. Using the Ultrafast Spectroscopy Modeling Toolbox,[83] a second-order polynomial was fitted to the pump coherent artefact and was sufficient to correct the majority of the inherent spectral chirp of the white light probe. A sequential model was then applied in the Toolbox for SVD analysis and global fitting. Application of a parallel model leads to overfitting, which is made clear by the presence of compensating amplitudes in the fitted components (not shown).

ASSOCIATED CONTENT

Supporting Information

The Supporting Information is available free of charge at https://pubs.acs.org/doi/10.1021/jacs.3c02313.

Frame data processing and crystallographic analysis; crystallographic map generation procedures; 2019 rsEGFP2 OFF state and cryo-trapping experiment; quantum chemical modeling procedures; anomalous crystallographic maps for confirmation of chlorine atom; and quantum yield calculations for Cl-rsEGFP2 (PDF)

AUTHOR INFORMATION

Corresponding Authors

Eriko Nango − *RIKEN Spring-8 Center, Sayo, Hyogo 679-5148, Japan; Institute of Multidisciplinary Research for*

https://doi.org/10.1021/jacs.3c02313
J. Am. Chem. Soc. 2023, 145, 15796−15808

Advanced Materials, Tohoku University, Sendai, Miyagi 980-8577, Japan; Email: eriko.nango.c4@tohoku.ac.jp
Jasper J. van Thor − *Department of Life Sciences, Faculty of Natural Sciences, Imperial College London, London SW7 2AZ, U.K.*; orcid.org/0000-0001-6356-3116; Email: j.vanthor@imperial.ac.uk

Authors

Alisia Fadini − *Department of Life Sciences, Faculty of Natural Sciences, Imperial College London, London SW7 2AZ, U.K.*
Christopher D.M. Hutchison − *Department of Life Sciences, Faculty of Natural Sciences, Imperial College London, London SW7 2AZ, U.K.*
Dmitry Morozov − *Nanoscience Center and Department of Chemistry, University of Jyväskylä, Jyväskylä 40014, Finland*; orcid.org/0000-0001-9524-948X
Jeffrey Chang − *Department of Physics, Stanford University, Stanford, California 94305, United States*; Present Address: Harvard University, Cambridge, Massachusetts 02138, United States
Karim Maghlaoui − *Department of Life Sciences, Faculty of Natural Sciences, Imperial College London, London SW7 2AZ, U.K.*
Samuel Perrett − *Department of Life Sciences, Faculty of Natural Sciences, Imperial College London, London SW7 2AZ, U.K.*; orcid.org/0000-0002-6728-0778
Fangjia Luo − *RIKEN Spring-8 Center, Sayo, Hyogo 679-5148, Japan*
Jeslyn C.X. Kho − *Department of Life Sciences, Faculty of Natural Sciences, Imperial College London, London SW7 2AZ, U.K.*
Matthew G. Romei − *Department of Chemistry, Stanford University, Stanford, California 94305, United States*; Present Address: Genentech Inc, South San Francisco, California 94080, United States
R. Marc L. Morgan − *Department of Life Sciences, Faculty of Natural Sciences, Imperial College London, London SW7 2AZ, U.K.*
Christian M. Orr − *Diamond Light Source Ltd, Harwell Science & Innovation Campus, Didcot OX11 0DE, U.K.*
Violeta Cordon-Preciado − *Department of Life Sciences, Faculty of Natural Sciences, Imperial College London, London SW7 2AZ, U.K.*
Takaaki Fujiwara − *Institute of Multidisciplinary Research for Advanced Materials, Tohoku University, Sendai, Miyagi 980-8577, Japan*
Nipawan Nuemket − *RIKEN Spring-8 Center, Sayo, Hyogo 679-5148, Japan; Department of Cell Biology, Graduate School of Medicine, Kyoto University, Kyoto 606-8501, Japan*
Takehiko Tosha − *RIKEN Spring-8 Center, Sayo, Hyogo 679-5148, Japan*; orcid.org/0000-0002-8971-0759
Rie Tanaka − *RIKEN Spring-8 Center, Sayo, Hyogo 679-5148, Japan; Department of Cell Biology, Graduate School of Medicine, Kyoto University, Kyoto 606-8501, Japan*
Shigeki Owada − *RIKEN Spring-8 Center, Sayo, Hyogo 679-5148, Japan; Japan Synchrotron Radiation Research Institute, Sayo, Hyogo 679-5198, Japan*
Kensuke Tono − *RIKEN Spring-8 Center, Sayo, Hyogo 679-5148, Japan; Japan Synchrotron Radiation Research Institute, Sayo, Hyogo 679-5198, Japan*
So Iwata − *RIKEN Spring-8 Center, Sayo, Hyogo 679-5148, Japan; Department of Cell Biology, Graduate School of Medicine, Kyoto University, Kyoto 606-8501, Japan*
Steven G. Boxer − *Department of Chemistry, Stanford University, Stanford, California 94305, United States*; orcid.org/0000-0001-9167-4286
Gerrit Groenhof − *Nanoscience Center and Department of Chemistry, University of Jyväskylä, Jyväskylä 40014, Finland*; orcid.org/0000-0001-8148-5334

Complete contact information is available at: https://pubs.acs.org/10.1021/jacs.3c02313

Notes

The authors declare no competing financial interest.

■ ACKNOWLEDGMENTS

The XFEL experiments were performed at SACLA BL3 with the approval of the Japan Synchrotron Radiation Research Institute (JASRI) (proposal nos. 2021A8006 and 22019B8021). JJvT and AF acknowledge funding from the Imperial College President's PhD Scholarship and the Biotechnology and Biological Sciences Research Council (BBSRC) (BB/P00752X/1). GG and DM acknowledge funding from the academy of Finland (grant no. 332743). This work was supported in part by a National Institutes of Health Grant (no. R35GM118044 to SGB). This work was also supported by the Japan Society for the Promotion of Science KAKENHI grants no. 19H05781 (E.N.) and 19H05776 (S. I.); the Platform Project for Supporting Drug Discovery and Life Science Research from the Japan Agency for Medical Research and Development under grant no. JP21am0101070 (S. I.). Use of the Stanford Synchrotron Radiation Lightsource, SLAC National Accelerator Laboratory, is supported by the U.S. Department of Energy (DOE), Office of Science, Office of Basic Energy Sciences (contract no. DE-AC02-76SF00515). The SSRL Structural Molecular Biology Program is supported by the DOE Office of Biological and Environmental Research and by the National Institutes of Health (NIH), National Institute of General Medical Sciences (NIGMS) (including P41GM103393). The contents of this publication are solely the responsibility of the authors and do not necessarily represent the official views of the NIGMS or NIH. We acknowledge TJ Lane for suggestion and discussion on the background subtraction estimation. We also thank Irimpan Matthews for assistance in the data collection at SSRL and acknowledge Diamond Light Source for time on I23 under proposal 23620. The crystallization facility at Imperial College was funded by BBSRC (BB/D524840/1) and the Wellcome Trust (202926/Z/16/Z).

■ REFERENCES

(1) Gozem, S.; Luk, H. L.; Schapiro, I.; Olivucci, M. Theory and Simulation of the Ultrafast Double-Bond Isomerization of Biological Chromophores. *Chem. Rev.* **2017**, *117*, 13502−13565.
(2) Kandori, H. Retinal Proteins: Photochemistry and Optogenetics. *Bull. Chem. Soc. Jpn.* **2020**, *93*, 76−85.
(3) Zhou, X. X.; Lin, M. Z. Photoswitchable fluorescent proteins: ten years of colorful chemistry and exciting applications. *Curr. Opin. Chem. Biol.* **2013**, *17*, 682−690.
(4) Cheng, M.-C.; Kathare, P. K.; Paik, I.; Huq, E. Phytochrome Signaling Networks. *Annu. Rev. Plant Biol.* **2021**, *72*, 217−244.
(5) Mishra, K.; Fuenzalida-Werner, J. P.; Pennacchietti, F.; Janowski, R.; Chmyrov, A.; Huang, Y.; Zakian, C.; Klemm, U.; Testa, I.; Niessing, D.; et al. Genetically encoded photo-switchable molecular sensors for optoacoustic and super-resolution imaging. *Nat. Biotechnol.* **2022**, *40*, 598−605.

(6) Dertinger, T.; Colyer, R.; Iyer, G.; Weiss, S.; Enderlein, J. Fast, background-free, 3D super-resolution optical fluctuation imaging (SOFI). *Proc. Natl. Acad. Sci. U.S.A.* **2009**, *106*, 22287−22292.
(7) Gustafsson, M. G. L. Nonlinear structured-illumination microscopy: wide-field fluorescence imaging with theoretically unlimited resolution. *Proc. Natl. Acad. Sci. U.S.A.* **2005**, *102*, 13081−13086.
(8) Brakemann, T.; Stiel, A. C.; Weber, G.; Andresen, M.; Testa, I.; Grotjohann, T.; Leutenegger, M.; Plessmann, U.; Urlaub, H.; Eggeling, C.; et al. A reversibly photoswitchable GFP-like protein with fluorescence excitation decoupled from switching. *Nat. Biotechnol.* **2011**, *29*, 942−947.
(9) Boyden, E. S.; Zhang, F.; Bamberg, E.; Nagel, G.; Deisseroth, K. Millisecond-timescale, genetically targeted optical control of neural activity. *Nat. Neurosci.* **2005**, *8*, 1263−1268.
(10) Lungu, O. I.; Hallett, R.; Choi, E.; Aiken, M.; Hahn, K.; Kuhlman, B. Designing photoswitchable peptides using the AsLOV2 domain. *Chem. Biol.* **2012**, *19*, 926−1017.
(11) Strickland, D.; Lin, Y.; Wagner, E.; Hope, C. M.; Zayner, J.; Antoniou, C.; Sosnick, T. R.; Weiss, E. L.; Glotzer, M. TULIPs: tunable, light-controlled interacting protein tags for cell biology. *Nat. Methods* **2012**, *9*, 379−384.
(12) Levskaya, A.; Weiner, O. D.; Lim, W. A.; Voigt, C. A. Spatiotemporal control of cell signalling using a light-switchable protein interaction. *Nature* **2009**, *461*, 997−1001.
(13) Müller, K.; Weber, W. Optogenetic tools for mammalian systems. *Mol. Biosyst.* **2013**, *9*, 596−608.
(14) Mo, G. C. H.; Posner, C.; Rodriguez, E. A.; Sun, T.; Zhang, J. A rationally enhanced red fluorescent protein expands the utility of FRET biosensors. *Nat. Commun.* **2020**, *11*, 1848.
(15) Wang, Q.; Byrnes, L. J.; Shui, B.; Röhrig, U. F.; Singh, A.; Chudakov, D. M.; Lukyanov, S.; Zipfel, W. R.; Kotlikoff, M. I.; Sondermann, H. Molecular Mechanism of a Green-Shifted, pH-Dependent Red Fluorescent Protein mKate Variant. *PLoS One* **2011**, *6*, No. e23513.
(16) Andresen, M.; Wahl, M. C.; Stiel, A. C.; Gräter, F.; Schäfer, L. V.; Trowitzsch, S.; Weber, G.; Eggeling, C.; Grubmüller, H.; Hell, S. W.; et al. Structure and mechanism of the reversible photoswitch of a fluorescent protein. *Proc. Natl. Acad. Sci. U.S.A.* **2005**, *102*, 13070−13074.
(17) Liu, R. S. H.; Hammond, G. S. The case of medium-dependent dual mechanisms for photoisomerization: One-bond-flip and Hula-Twist. *Proc. Natl. Acad. Sci. U.S.A.* **2000**, *97*, 11153−11158.
(18) Liu, R. S.; Asato, A. E. The primary process of vision and the structure of bathorhodopsin: a mechanism for photoisomerization of polyenes. *Proc. Natl. Acad. Sci. U.S.A.* **1985**, *82*, 259−263.
(19) Warshel, A. Bicycle-pedal model for the first step in the vision process. *Nature* **1976**, *260*, 679−683.
(20) Schapiro, I.; Weingart, O.; Buss, V. Bicycle-Pedal Isomerization in a Rhodopsin Chromophore Model. *J. Am. Chem. Soc.* **2009**, *131*, 16−17.
(21) Altoè, P.; Cembran, A.; Olivucci, M.; Garavelli, M. Aborted double bicycle-pedal isomerization with hydrogen bond breaking is the primary event of bacteriorhodopsin proton pumping. *Proc. Natl. Acad. Sci. U.S.A.* **2010**, *107*, 20172−20177.
(22) Gruhl, T.; Weinert, T.; Rodrigues, M. J.; Milne, C. J.; Ortolani, G.; Nass, K.; Nango, E.; Sen, S.; Johnson, P. J. M.; Cirelli, C.; et al. Ultrafast structural changes direct the first molecular events of vision. *Nature* **2023**, *615*, 939−944.
(23) Frutos, L. M.; Andruniów, T.; Santoro, F.; Ferré, N.; Olivucci, M. Tracking the excited-state time evolution of the visual pigment with multiconfigurational quantum chemistry. *Proc. Natl. Acad. Sci. U.S.A.* **2007**, *104*, 7764−7769.
(24) Jung, Y. O.; Lee, J. H.; Kim, J.; Schmidt, M.; Moffat, K.; Šrajer, V.; Ihee, H. Volume-conserving trans−cis isomerization pathways in photoactive yellow protein visualized by picosecond X-ray crystallography. *Nat. Chem.* **2013**, *5*, 212−220.
(25) Liu, R. S. H. Introduction to the Symposium-in-print: Photoisomerization Pathways, Torsional Relaxation and the Hula Twist. *Photochem. Photobiol.* **2007**, *76*, 580−583.
(26) Gayda, S.; Nienhaus, K.; Nienhaus, G. U. Mechanistic insights into reversible photoactivation in proteins of the GFP family. *Biophys. J.* **2012**, *103*, 2521−2531.
(27) Schäfer, L. V.; Groenhof, G.; Boggio-Pasqua, M.; Robb, M. A.; Grubmüller, H. Chromophore Protonation State Controls Photoswitching of the Fluoroprotein asFP595. *PLoS Comput. Biol.* **2008**, *4*, No. e1000034.
(28) Li, X.; Chung, L. W.; Mizuno, H.; Miyawaki, A.; Morokuma, K. Primary events of photodynamics in reversible photoswitching fluorescent protein dronpa. *J. Phys. Chem. Lett.* **2010**, *1*, 3328−3333.
(29) Jonasson, G.; Teuler, J. M.; Vallverdu, G.; Mérola, F.; Ridard, J.; Lévy, B.; Demachy, I. Excited State Dynamics of the Green Fluorescent Protein on the Nanosecond Time Scale. *J. Chem. Theory Comput.* **2011**, *7*, 1990−1997.
(30) Zhang, Q.; Chen, X.; Cui, G.; Fang, W.-H.; Thiel, W. Concerted Asynchronous Hula-Twist Photoisomerization in the S65T/H148D Mutant of Green Fluorescent Protein. *Angew. Chem.* **2014**, *126*, 8793−8797.
(31) Maddalo, S. L.; Zimmer, M. The Role of the Protein Matrix in Green Fluorescent Protein Fluorescence. *Photochem. Photobiol.* **2006**, *82*, 367.
(32) Acharya, A.; Bogdanov, A. M.; Grigorenko, B. L.; Bravaya, K. B.; Nemukhin, A. V.; Lukyanov, K. A.; Krylov, A. I. Photoinduced Chemistry in Fluorescent Proteins: Curse or Blessing? *Chem. Rev.* **2017**, *117*, 758−795.
(33) Grotjohann, T.; Testa, I.; Reuss, M.; Brakemann, T.; Eggeling, C.; Hell, S. W.; Jakobs, S. rsEGFP2 enables fast RESOLFT nanoscopy of living cells. *Elife* **2012**, *1*, No. e00248.
(34) Hofmann, M.; Eggeling, C.; Jakobs, S.; Hell, S. W. Breaking the diffraction barrier in fluorescence microscopy at low light intensities by using reversibly photoswitchable proteins. *Proc. Natl. Acad. Sci. U.S.A.* **2005**, *102*, 17565−17569.
(35) Bourgeois, D.; Adam, V. Reversible photoswitching in fluorescent proteins: A mechanistic view. *IUBMB Life* **2012**, *64*, 482−491.
(36) Sahl, S. J.; Hell, S. W.; Jakobs, S. Fluorescence nanoscopy in cell biology. *Nat. Rev. Mol. Cell Biol.* **2017**, *18*, 685−701.
(37) Sigal, Y. M.; Zhou, R.; Zhuang, X. Visualizing and discovering cellular structures with super-resolution microscopy. *Science* **2018**, *361*, 880−887.
(38) Schnorrenberg, S.; Grotjohann, T.; Vorbrüggen, G.; Herzig, A.; Hell, S. W.; Jakobs, S. In vivo super-resolution RESOLFT microscopy of Drosophila melanogaster. *Elife* **2016**, *5*, No. e15567.
(39) Shroff, H.; Galbraith, C. G.; Galbraith, J. A.; Betzig, E. Live-cell photoactivated localization microscopy of nanoscale adhesion dynamics. *Nat. Methods* **2008**, *5*, 417−423.
(40) Dertinger, T.; Colyer, R.; Iyer, G.; Weiss, S.; Enderlein, J. Fast, background-free, 3D super-resolution optical fluctuation imaging (SOFI). *Proc. Natl. Acad. Sci. U.S.A.* **2009**, *106*, 22287−22292.
(41) Brakemann, T.; Stiel, A. C.; Weber, G.; Andresen, M.; Testa, I.; Grotjohann, T.; Leutenegger, M.; Plessmann, U.; Urlaub, H.; Eggeling, C.; et al. A reversibly photoswitchable GFP-like protein with fluorescence excitation decoupled from switching. *Nat. Biotechnol.* **2011**, *29*, 942−947.
(42) Grotjohann, T.; Testa, I.; Leutenegger, M.; Bock, H.; Urban, N. T.; Lavoie-Cardinal, F.; Willig, K. I.; Eggeling, C.; Jakobs, S.; Hell, S. W. Diffraction-unlimited all-optical imaging and writing with a photochromic GFP. *Nature* **2011**, *478*, 204−208.
(43) El Khatib, M.; Martins, A.; Bourgeois, D.; Colletier, J.-P.; Adam, V. Rational design of ultrastable and reversibly photoswitchable fluorescent proteins for super-resolution imaging of the bacterial periplasm. *Sci. Rep.* **2016**, *6*, 18459.
(44) Woodhouse, J.; Nass Kovacs, G.; Coquelle, N.; Uriarte, L. M.; Adam, V.; Barends, T. R. M.; Byrdin, M.; de la Mora, E.; Bruce Doak, R.; Feliks, M.; et al. Photoswitching mechanism of a fluorescent

https://doi.org/10.1021/jacs.3c02313
J. Am. Chem. Soc. 2023, 145, 15796−15808

protein revealed by time-resolved crystallography and transient absorption spectroscopy. *Nat. Commun.* **2020**, *11*, 741.
(45) Coquelle, N.; Sliwa, M.; Woodhouse, J.; Schirò, G.; Adam, V.; Aquila, A.; Barends, T. R. M.; Boutet, S.; Byrdin, M.; Carbajo, S.; et al. Chromophore twisting in the excited state of a photoswitchable fluorescent protein captured by time-resolved serial femtosecond crystallography. *Nat. Chem.* **2018**, *10*, 31−37.
(46) Ando, R.; Mizuno, H.; Miyawaki, A. Regulated fast nucleocytoplasmic shuttling observed by reversible protein highlighting. *Science* **2004**, *306*, 1370−1373.
(47) Romei, M. G.; Lin, C.-Y.; Boxer, S. G. Structural and spectroscopic characterization of photoactive yellow protein and photoswitchable fluorescent protein constructs containing heavy atoms. *J. Photochem. Photobiol., A* **2020**, *401*, 112738.
(48) Chang, J.; Romei, M. G.; Boxer, S. G. Structural Evidence of Photoisomerization Pathways in Fluorescent Proteins. *J. Am. Chem. Soc.* **2019**, *141*, 15504−15508.
(49) Moss, G. P. Basic terminology of stereochemistry (IUPAC Recommendations 1996). *Pure Appl. Chem.* **1996**, *68*, 2193−2222.
(50) Muller, P. Glossary of terms used in physical organic chemistry (IUPAC Recommendations 1994). *Pure Appl. Chem.* **1994**, *66*, 1077−1184.
(51) Cahn, R. S.; Ingold, C.; Prelog, V. Specification of Molecular Chirality. *Angew. Chem., Int. Ed. Engl.* **1966**, *5*, 385−415.
(52) Adam, V.; Hadjidemetriou, K.; Jensen, N.; Shoeman, R. L.; Woodhouse, J.; Aquila, A.; Banneville, A.; Barends, T. R. M.; Bezchastnov, V.; Boutet, S.; et al. Rational Control of Off-State Heterogeneity in a Photoswitchable Fluorescent Protein Provides Switching Contrast Enhancement. *ChemPhysChem* **2022**, *23*, No. e202200192.
(53) Pearce, N. M.; Krojer, T.; Bradley, A. R.; Collins, P.; Nowak, R. P.; Talon, R.; Marsden, B. D.; Kelm, S.; Shi, J.; Deane, C. M.; et al. A multi-crystal method for extracting obscured crystallographic states from conventionally uninterpretable electron density. *Nat. Commun.* **2017**, *8*, 15123.
(54) Pande, K.; Hutchison, C. D. M.; Groenhof, G.; Aquila, A.; Robinson, J. S.; Tenboer, J.; Basu, S.; Boutet, S.; DePonte, D. P.; Liang, M.; et al. Femtosecond structural dynamics drives the trans/cis isomerization in photoactive yellow protein. *Science* **2016**, *352*, 725−729.
(55) Wickstrand, C.; Katona, G.; Nakane, T.; Nogly, P.; Standfuss, J.; Nango, E.; Neutze, R. A tool for visualizing protein motions in time-resolved crystallography. *Struct. Dyn.* **2020**, *7*, 024701.
(56) Lelimousin, M.; Noirclerc-Savoye, M.; Lazareno-Saez, C.; Paetzold, B.; Le Vot, S.; Chazal, R.; Macheboeuf, P.; Field, M. J.; Bourgeois, D.; Royant, A. Intrinsic dynamics in ECFP and Cerulean control fluorescence quantum yield. *Biochemistry* **2009**, *48*, 10038−10046.
(57) Shinobu, A.; Agmon, N. The hole in the barrel: water exchange at the GFP chromophore. *J. Phys. Chem. B* **2015**, *119*, 3464−3478.
(58) Mizuno, H.; Mal, T. K.; Wälchli, M.; Kikuchi, A.; Fukano, T.; Ando, R.; Jeyakanthan, J.; Taka, J.; Shiro, Y.; Ikura, M.; et al. Light-dependent regulation of structural flexibility in a photochromic fluorescent protein. *Proc. Natl. Acad. Sci. U.S.A.* **2008**, *105*, 9227−9232.
(59) Seifert, M. H. J.; Georgescu, J.; Ksiazek, D.; Smialowski, P.; Rehm, T.; Steipe, B.; Holak, T. A. Backbone dynamics of green fluorescent protein and the effect of histidine 148 substitution. *Biochemistry* **2003**, *42*, 2500−2512.
(60) Christou, N.-E.; Ayala, I.; Giandoreggio-Barranco, K.; Byrdin, M.; Adam, V.; Bourgeois, D.; Brutscher, B. NMR Reveals Light-Induced Changes in the Dynamics of a Photoswitchable Fluorescent Protein. *Biophys. J.* **2019**, *117*, 2087−2100.
(61) Uriarte, L. M.; Vitale, R.; Niziński, S.; Hadjidemetriou, K.; Zala, N.; Lukacs, A.; Greetham, G. M.; Sazanovich, I. V.; Weik, M.; Ruckebusch, C.; et al. Structural Information about the trans -to- cis Isomerization Mechanism of the Photoswitchable Fluorescent Protein rsEGFP2 Revealed by Multiscale Infrared Transient Absorption. *J. Phys. Chem. Lett.* **2022**, *13*, 1194−1202.
(62) Boeije, Y.; Olivucci, M. From a one-mode to a multi-mode understanding of conical intersection mediated ultrafast organic photochemical reactions. *Chem. Soc. Rev.* **2023**, *52*, 2643−2687.
(63) Grigorenko, B. L.; Domratcheva, T.; Polyakov, I. V.; Nemukhin, A. V. Protonation States of Molecular Groups in the Chromophore-Binding Site Modulate Properties of the Reversibly Switchable Fluorescent Protein rsEGFP2. *J. Phys. Chem. Lett.* **2021**, *12*, 8263−8271.
(64) Polyakov, I. V.; Grigorenko, B. L.; Epifanovsky, E. M.; Krylov, A. I.; Nemukhin, A. V. Potential Energy Landscape of the Electronic States of the GFP Chromophore in Different Protonation Forms: Electronic Transition Energies and Conical Intersections. *J. Chem. Theory Comput.* **2010**, *6*, 2377−2387.
(65) Polli, D.; Altoè, P.; Weingart, O.; Spillane, K. M.; Manzoni, C.; Brida, D.; Tomasello, G.; Orlandi, G.; Kukura, P.; Mathies, R. A.; et al. Conical intersection dynamics of the primary photoisomerization event in vision. *Nature* **2010**, *467*, 440−443.
(66) Wang, Q.; Schoenlein, R. W.; Peteanu, L. A.; Mathies, R. A.; Shank, C. V. Vibrationally coherent photochemistry in the femtosecond primary event of vision. *Science* **1994**, *266*, 422−424.
(67) Prokhorenko, V. I.; Nagy, A. M.; Waschuk, S. A.; Brown, L. S.; Birge, R. R.; Miller, R. J. D. Coherent Control of Retinal Isomerization in Bacteriorhodopsin. *Science* **2006**, *313*, 1257−1261.
(68) Liebel, M.; Schnedermann, C.; Bassolino, G.; Taylor, G.; Watts, A.; Kukura, P. Direct observation of the coherent nuclear response after the absorption of a photon. *Phys. Rev. Lett.* **2014**, *112*, 238301.
(69) Florean, A. C.; Cardoza, D.; White, J. L.; Lanyi, J. K.; Sension, R. J.; Bucksbaum, P. H. Control of retinal isomerization in bacteriorhodopsin in the high-intensity regime. *Proc. Natl. Acad. Sci. U.S.A.* **2009**, *106*, 10896−10900.
(70) Litvinenko, K. L.; Meech, S. R. Observation of low frequency vibrational modes in a mutant of the green fluorescent protein. *Phys. Chem. Chem. Phys.* **2004**, *6*, 2012.
(71) Cinelli, R. A. G.; Tozzini, V.; Pellegrini, V.; Beltram, F.; Cerullo, G.; Zavelani-Rossi, M.; De Silvestri, S.; Tyagi, M.; Giacca, M. Coherent Dynamics of Photoexcited Green Fluorescent Proteins. *Phys. Rev. Lett.* **2001**, *86*, 3439−3442.
(72) Fujisawa, T.; Kuramochi, H.; Hosoi, H.; Takeuchi, S.; Tahara, T. Role of Coherent Low-Frequency Motion in Excited-State Proton Transfer of Green Fluorescent Protein Studied by Time-Resolved Impulsive Stimulated Raman Spectroscopy. *J. Am. Chem. Soc.* **2016**, *138*, 3942−3945.
(73) Mukherjee, S.; Hung, S. T.; Douglas, N.; Manna, P.; Thomas, C.; Ekrem, A.; Palmer, A. E.; Jimenez, R. Engineering of a Brighter Variant of the FusionRed Fluorescent Protein Using Lifetime Flow Cytometry and Structure-Guided Mutations. *Biochemistry* **2020**, *59*, 3669−3682.
(74) Mohr, M. A.; Kobitski, A. Y.; Sabater, L. R.; Nienhaus, K.; Obara, C. J.; Lippincott-Schwartz, J.; Nienhaus, G. U.; Pantazis, P. Rational Engineering of Photoconvertible Fluorescent Proteins for Dual-Color Fluorescence Nanoscopy Enabled by a Triplet-State Mechanism of Primed Conversion. *Angew. Chem., Int. Ed. Engl.* **2017**, *56*, 11628−11633.
(75) Tsutsui, H.; Karasawa, S.; Shimizu, H.; Nukina, N.; Miyawaki, A. Semi-rational engineering of a coral fluorescent protein into an efficient highlighter. *EMBO Rep.* **2005**, *6*, 233−238.
(76) Mafuné, F.; Miyajima, K.; Tono, K.; Takeda, Y.; Kohno, J. y.; Miyauchi, N.; Kobayashi, J.; Joti, Y.; Nango, E.; Iwata, S.; et al. Microcrystal delivery by pulsed liquid droplet for serial femtosecond crystallography. *Acta Crystallogr., Sect. D: Struct. Biol.* **2016**, *72*, 520−523.
(77) Ishikawa, T.; Aoyagi, H.; Asaka, T.; Asano, Y.; Azumi, N.; Bizen, T.; Ego, H.; Fukami, K.; Fukui, T.; Furukawa, Y.; et al. A compact X-ray free-electron laser emitting in the sub-ångström region. *Nat. Photonics* **2012**, *6*, 540−544.
(78) Kameshima, T.; Ono, S.; Kudo, T.; Ozaki, K.; Kirihara, Y.; Kobayashi, K.; Inubushi, Y.; Yabashi, M.; Horigome, T.; Holland, A.; et al. Development of an X-ray pixel detector with multi-port charge-

https://doi.org/10.1021/jacs.3c02313
J. Am. Chem. Soc. 2023, 145, 15796−15808

coupled device for X-ray free-electron laser experiments. *Rev. Sci. Instrum.* **2014**, *85*, 033110.
(79) Sanchez-Gonzalez, A.; Johnson, A. S.; Fitzpatrick, A.; Hutchison, C. D. M.; Fare, C.; Cordon-Preciado, V.; Dorlhiac, G.; Ferreira, J. L.; Morgan, R. M.; Marangos, J. P.; et al. Coincidence timing of femtosecond optical pulses in an X-ray free electron laser. *J. Appl. Phys.* **2017**, *122*, 203105.
(80) Sato, T.; Togashi, T.; Ogawa, K.; Katayama, T.; Inubushi, Y.; Tono, K.; Yabashi, M. Highly efficient arrival timing diagnostics for femtosecond X-ray and optical laser pulses. *Appl. Phys. Express* **2015**, *8*, 012702.
(81) Togashi, T.; Owada, S.; Kubota, Y.; Sueda, K.; Katayama, T.; Tomizawa, H.; Yabuuchi, T.; Tono, K.; Yabashi, M. Femtosecond Optical Laser System with Spatiotemporal Stabilization for Pump-Probe Experiments at SACLA. *Appl. Sci.* **2020**, *10*, 7934.
(82) Lincoln, C. N.; Fitzpatrick, A. E.; van Thor, J. J. Photoisomerisation quantum yield and non-linear cross-sections with femtosecond excitation of the photoactive yellow protein. *Phys. Chem. Chem. Phys.* **2012**, *14*, 15752.
(83) van Wilderen, L. J. G. W.; Lincoln, C. N.; van Thor, J. J. Modelling Multi-Pulse Population Dynamics from Ultrafast Spectroscopy. *PLoS One* **2011**, *6*, No. e17373.

https://doi.org/10.1021/jacs.3c02313
J. Am. Chem. Soc. 2023, 145, 15796−15808

Serial Femtosecond Crystallography Reveals that Photoactivation in a Fluorescent Protein Proceeds via the Hula Twist Mechanism - Supporting Information

Authors:

Alisia Fadini[1], Christopher D.M. Hutchison[1], Dmitry Morozov[2], Jeffrey Chang[3], Karim Maghlaoui[1], Samuel Perrett[1], Fangjia Luo[4], Jeslyn C.X. Kho[1], Matthew G. Romei[5], R. Marc L. Morgan[1], Christian M. Orr[6], Violeta Cordon-Preciado[1], Takaaki Fujiwara[7], Nipawan Nuemket[4,8], Takehiko Tosha[4], Rie Tanaka[4,8], Shigeki Owada[4,9], Kensuke Tono[4,9], So Iwata[4,8], Steven G. Boxer[5], Gerrit Groenhof[2], Eriko Nango[4,7*], Jasper J. van Thor[1*]

Affiliations:

[1] Department of Life Sciences, Faculty of Natural Sciences, Imperial College London, London, SW7 2AZ, UK

[2] Nanoscience Center and Department of Chemistry, University of Jyväskylä, Jyväskylä, 40014, Finland

[3] Department of Physics, Stanford University, Stanford, CA 94305, USA

[4] RIKEN SPring-8 Center, 1-1-1 Kouto, Sayo, Sayo, Hyogo, 679-5148, Japan

[5] Department of Chemistry, Stanford University, Stanford, CA 94305, USA

[6] Diamond Light Source Ltd, Harwell Science and Innovation Campus, Didcot, OX11 0DE, UK

[7] Institute of Multidisciplinary Research for Advanced Materials, Tohoku University, 2-1-1 Katahira, Aoba, Sendai, Miyagi, 980-8577, Japan

[8] Department of Cell Biology, Graduate School of Medicine, Kyoto University, Yoshidakonoe, Sakyo, Kyoto, 606-8501, Japan

[9] Japan Synchrotron Radiation Research Institute, 1-1-1 Kouto, Sayo, Sayo, Hyogo, 679-5198, Japan

Supporting Figures and Tables

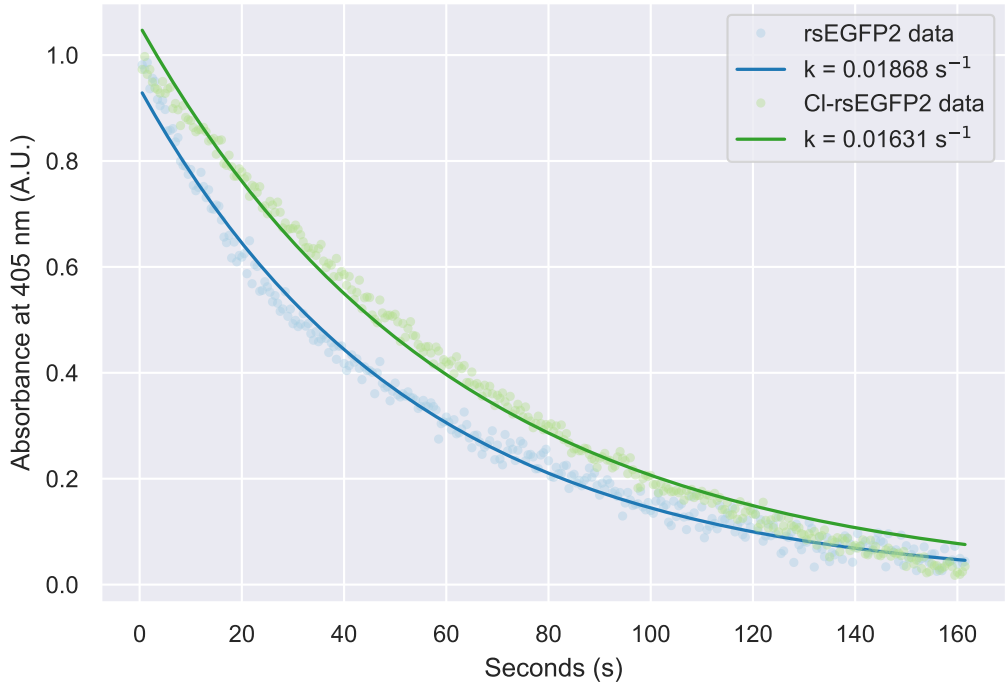

Figure S1. OFF-to-ON switching rates for chlorinated and unchlorinated rsEGFP2 constructs measured under the same conditions. An exponential decay of the form $y = Ae^{-kt}$ was fitted to obtain the rate k for each construct. Related to Figure 2.

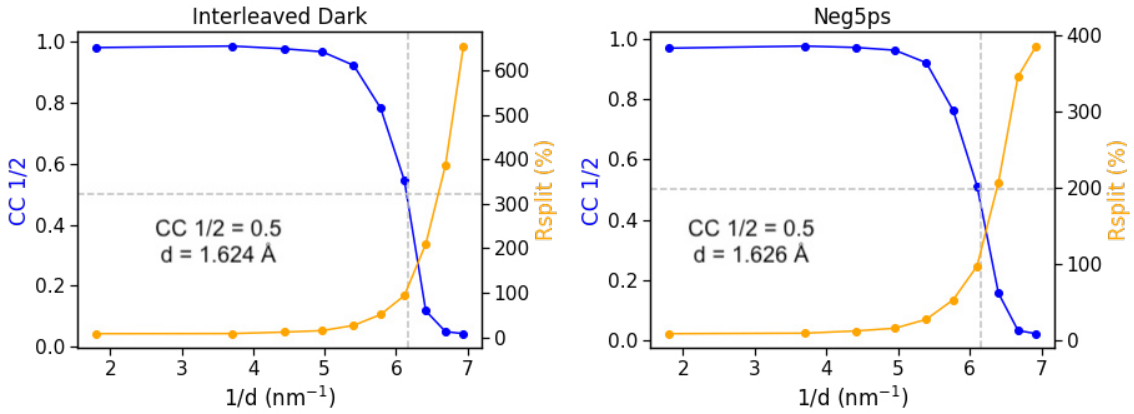

Figure S2. Choice of resolution cutoff from the dark SFX data. A $CC_{1/2}$ of 0.5 was chosen, corresponding to $\approx$ 1.63 Å for both the interleaved dark and -5ps datasets.

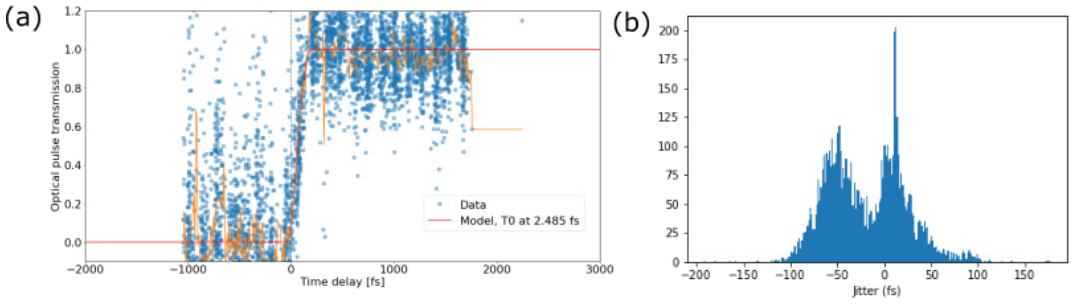

Figure S3. (a) Cross-correlation between the laser pump and XFEL probe for time zero determination and **(b)** jitter analysis for the SACLA 2021 experiment. Related to Figure 4.

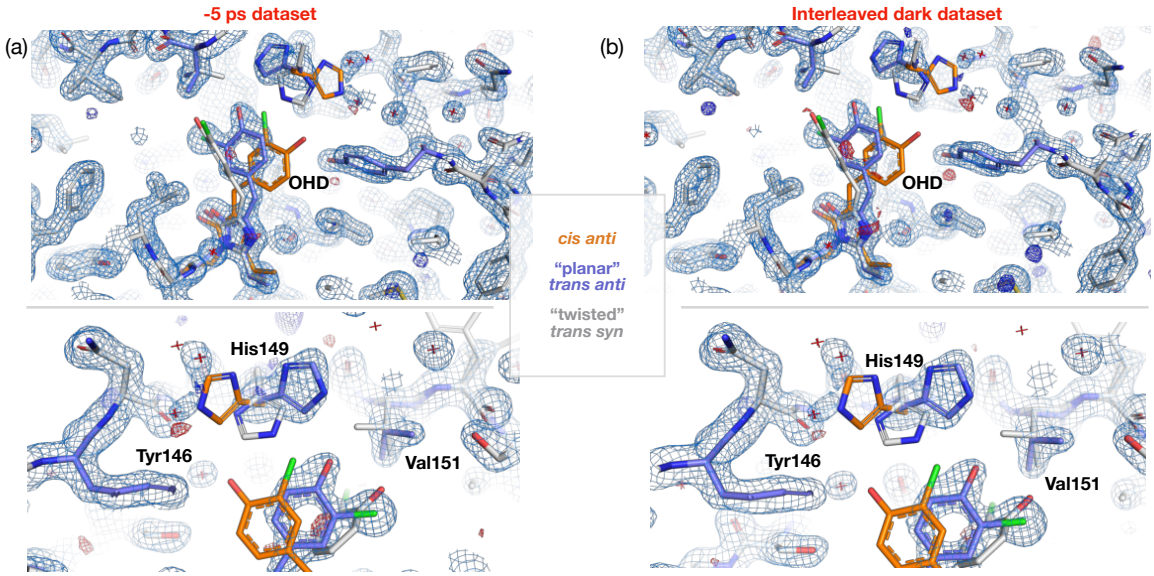

Figure S4. 2mFo-DFc maps, shown at +1.8σ, computed from the -5 ps **(a)** and interleaved dark **(b)** datasets and the refined dark structure (PDB 8A6G). mFo-DFc maps are shown in red and green at -3σ and +3σ respectively. The top and bottom panels show two different views of the chromophore (OHD) region. The three chromophore populations modeled in the dark state, planar *trans anti* (*trans-PL*), twisted *trans syn* (*trans-TW*), and *cis anti*, are shown in distinct colors with the corresponding interacting residue conformations. Related to Figure 3.

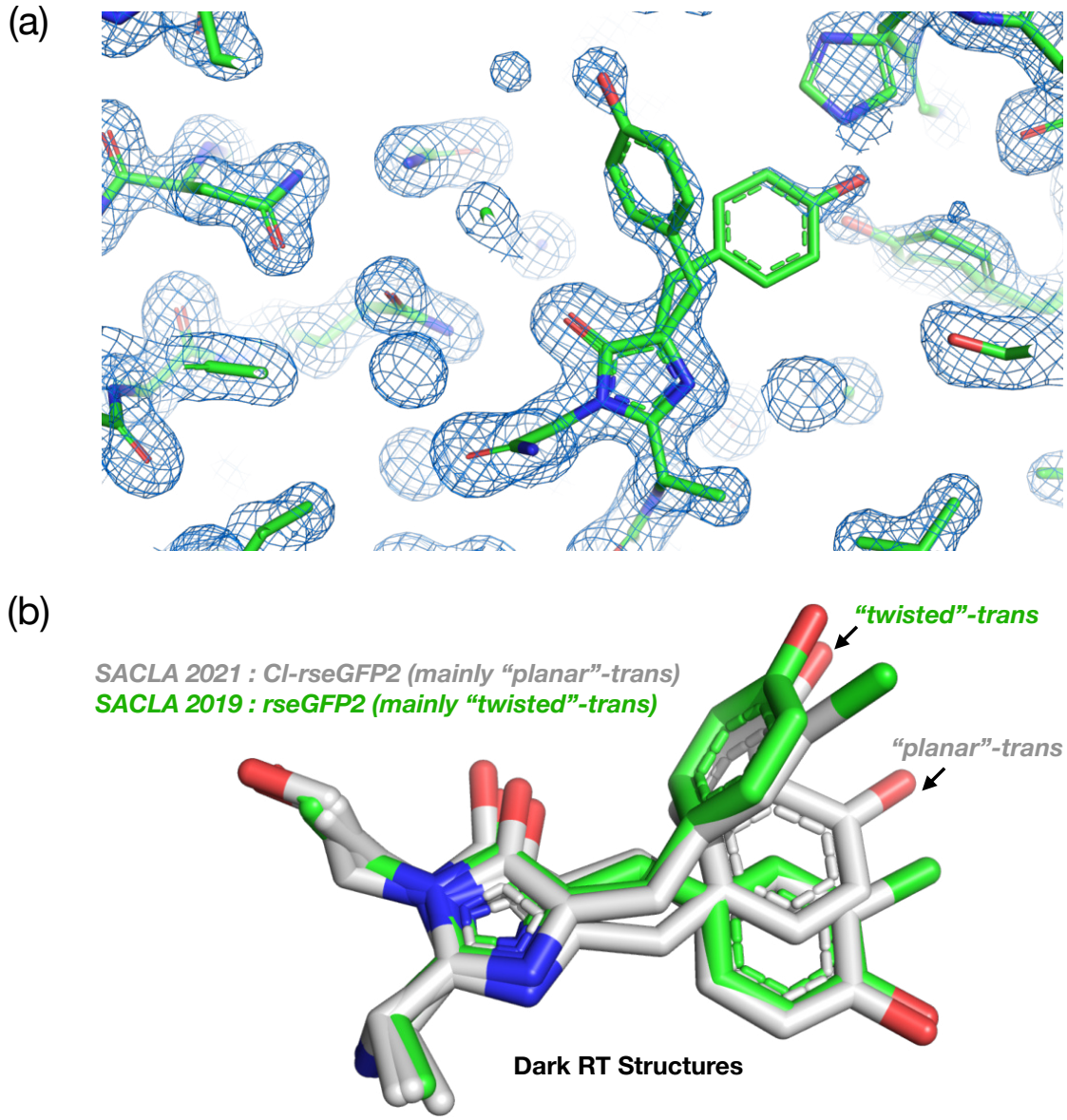

Figure S5. (a) 2mFo-DFc map, shown at 1.8σ, computed with the reflections from dark data collected on rsEGFP2 (unchlorinated) at SACLA in 2019 and the refined dark structure (PDB 8A7V). The prevalent chromophore conformation is the *trans*, though a small population of *cis* is also refined. **(b)** Superposition of the refined dark room temperature (RT) structures for the unchlorinated rsEGFP2 (SACLA 2019, green) and Cl-rsEGFP2 (SACLA 2021, gray). It is highlighted how the major chromophore *trans* configuration differs between the two: rsEGFP2 is found in the twisted *trans* configuration (*trans-TW*), while Cl-rsEGFP2 is mainly in the planar *trans* configuration (*trans-PL*). Both datasets present minor *cis* chromophore conformations. Related to Figure 3.

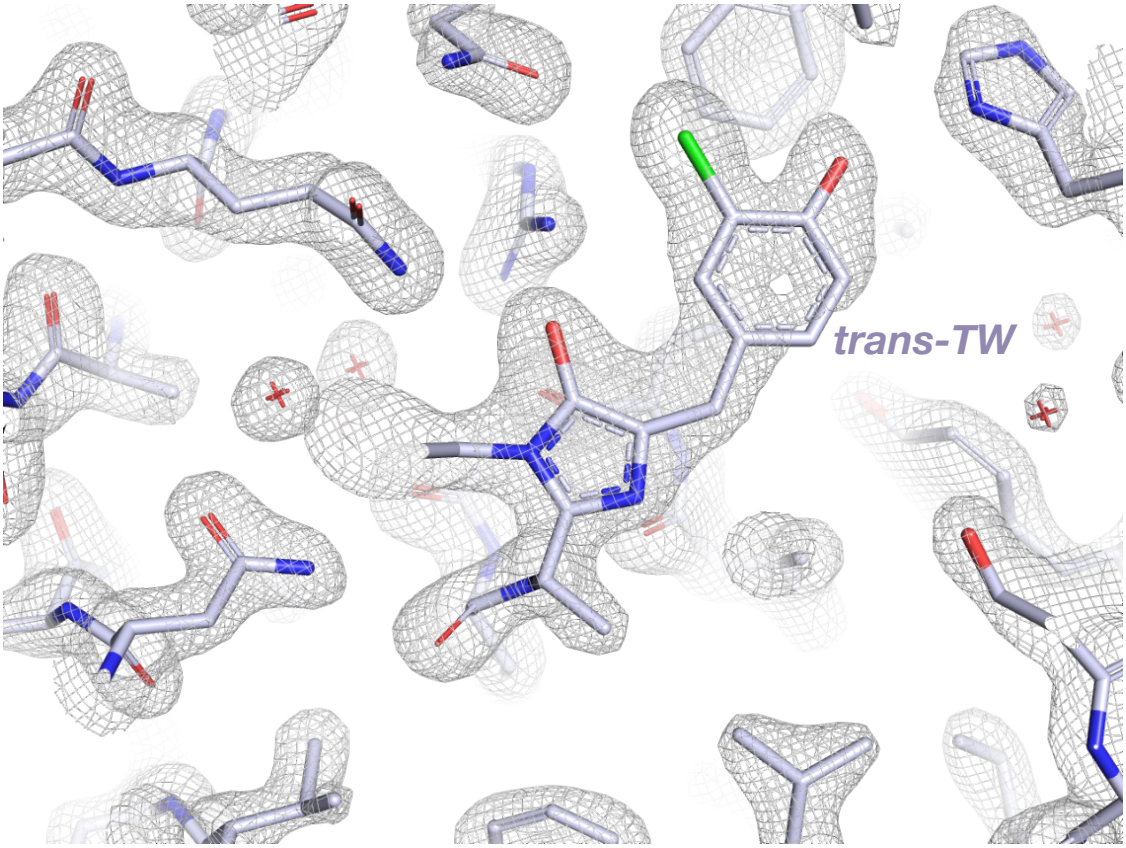

Figure S6. 2mFo-DFc map, shown at 1.8σ, computed with the reflections from data collected on Cl-rsEGFP2 at SSRL after illumination and dehydration and the refined structure (PDB 8A83). The prevalent chromophore conformation is *trans-PL*. Related to Figure 3.

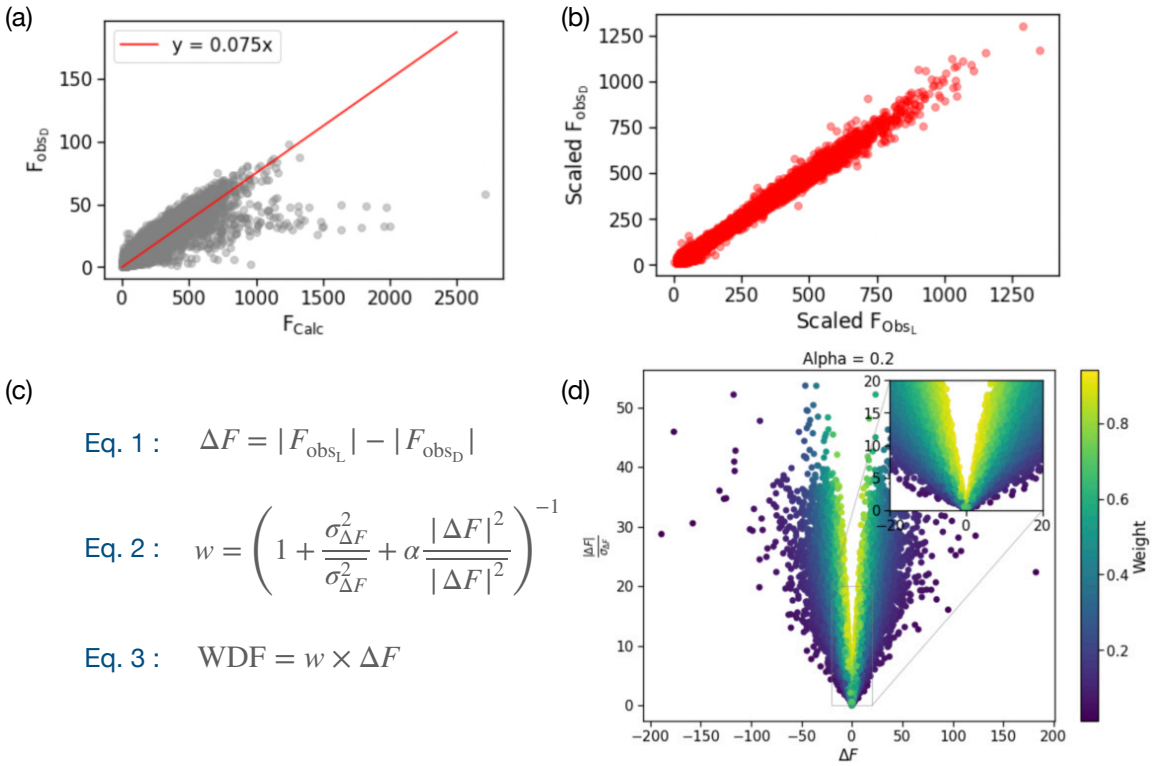

Figure S7. (a) Example of scale factor determination. The structure factors from the -5 ps dataset (F_{obs_D}) are plotted against structure factors from the refined dark model (F_{calc}) and a line of the form y = *m*x is fitted to the data. For the dark structure factors, *m* = 0.75. In the same manner, the light structure factors for every time point are scaled to F_{calc}. **(b)** Example of the result of scaling on dark (F_{obs_D}) and light (F_{obs_L}) structure factors (here the 100 ps dataset is shown). For the data presented in this work, this simple scaling procedure is sufficient to yield highly correlated light and dark structure factors. **(c)** Mathematical procedure to obtain weighted difference structure factors (WDF) from dark and light structure factors. $\sigma_{\Delta F}$ is the structure factor standard deviation and the term α reduces the contribution of any single ΔF. **(d)** Weights applied to the 100 ps dataset for α=0.2, shown as an example. Difference structure factors that are large or measured with a higher error are given progressively lower weight. Related to Figure 4.

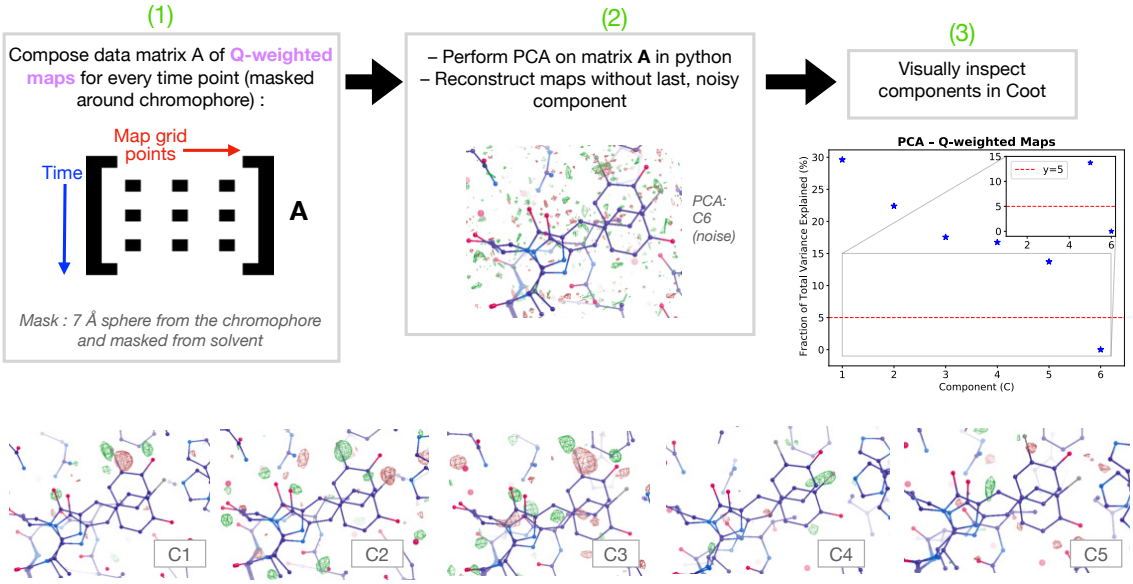

Figure S8. The pipeline implemented to denoise Q-weighted maps through PCA is shown. Each map from a collected time point is a row in the data matrix A (6 time points total: 300 fs, 600 fs, 900 fs, 5 ps, 100 ps, 1 μs) and PCA is performed using the sci-kit learn package in python. The last (C6) component found explains less than 5% of the total variance in the data and, upon visual inspection, appears as noise. The first five components are shown in the bottom panels at +/-3.5σ. Related to Figure 4.

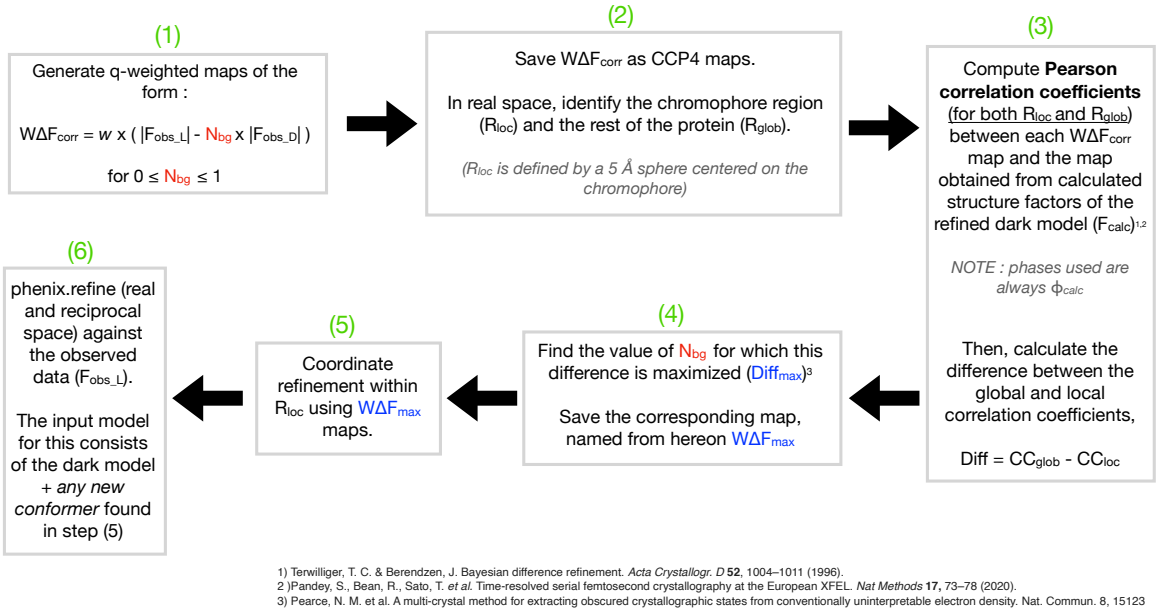

1) Terwilliger, T. C. & Berendzen, J. Bayesian difference refinement. *Acta Crystallogr. D* **52**, 1004–1011 (1996).
2)Pandey, S., Bean, R., Sato, T. *et al.* Time-resolved serial femtosecond crystallography at the European XFEL. *Nat Methods* **17,** 73–78 (2020).
3) Pearce, N. M. et al. A multi-crystal method for extracting obscured crystallographic states from conventionally uninterpretable electron density. Nat. Commun. 8, 15123

Figure S9. Schematic of the steps involved in the generation of background subtracted maps ($W\Delta F_{max}$ maps). Related to Figure 5.

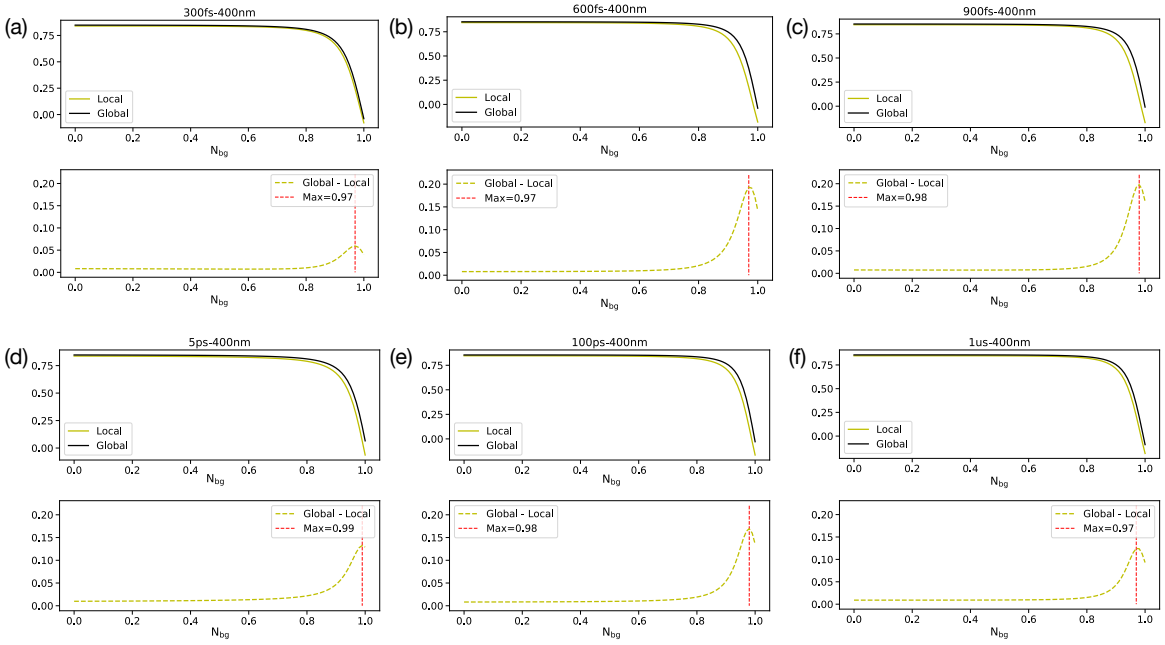

Figure S10. Identification of the appropriate background subtraction factor (N_{bg}) for the $W\Delta F_{max}$ map of each timepoint **(a-f)**. The top panels plot the correlation coefficient between the original and the background subtracted map for different N_{bg} values calculated across the entire protein structure (global) and a specific 5 Å sphere centered on the chromophore (local). The bottom panels plot the difference between the global and local lines and highlight the value of N_{bg} for which the difference in correlation coefficients is maximized. Related to Figures 4 and 5.

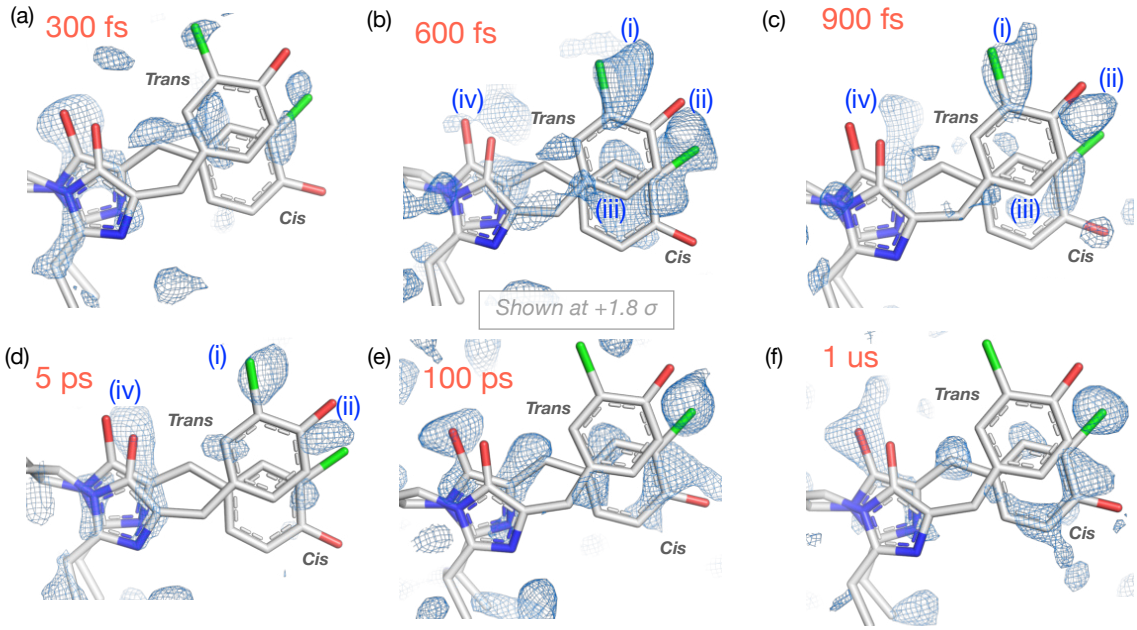

Figure S11. $W\Delta F_{max}$ maps generated using the method described in this work and illustrated in Figure S9. The following four characteristics, which we attribute to the presence of a femtosecond intermediate, are marked in the 600 fs and 900 fs maps: (i) the presence of Peak 1 (ii) an elongated and uncentered peak where the *cis anti* chlorine is positioned, which is in contrast with the round, centered features visible in the $W\Delta F_{max}$ maps from the later time points (iii) electron density that fills the *cis anti* chromophore phenol ring (iv) features that suggest a tilt of the imidazolidone ring oxygen towards the phenol ring. Though less pronounced, these features are also identifiable in the 5 ps map. Related to Figures 4 and 5.

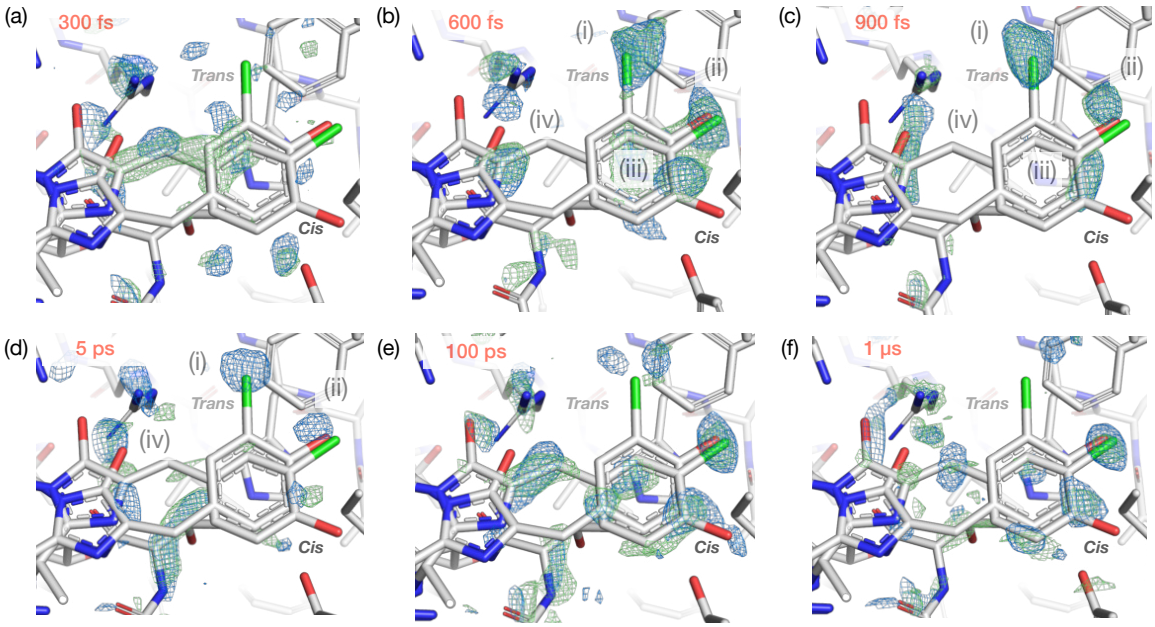

Figure S12. WΔF_{max} maps generated by subtraction of dark and light 2mFo-DFc maps, as described in Pearce *et al.*[1] (in green), overlaid with the WΔF_{max} maps from Figure S11 (in blue), both shown at +2.1σ. The two sets of maps largely overlap. The following four characteristics, which we attribute to the presence of a femtosecond intermediate, are marked in the 600 fs and 900 fs maps: (i) the presence of Peak 1 (ii) an elongated and uncentered peak where the *cis anti* chlorine is positioned, which is in contrast with the round, centered features visible in the WΔF_{max} maps from the later time points (iii) electron density that fills the *cis anti* chromophore phenol ring (iv) features that suggest a tilt of the imidazolidone ring oxygen towards the phenol ring. Related to Figures 4 and 5.

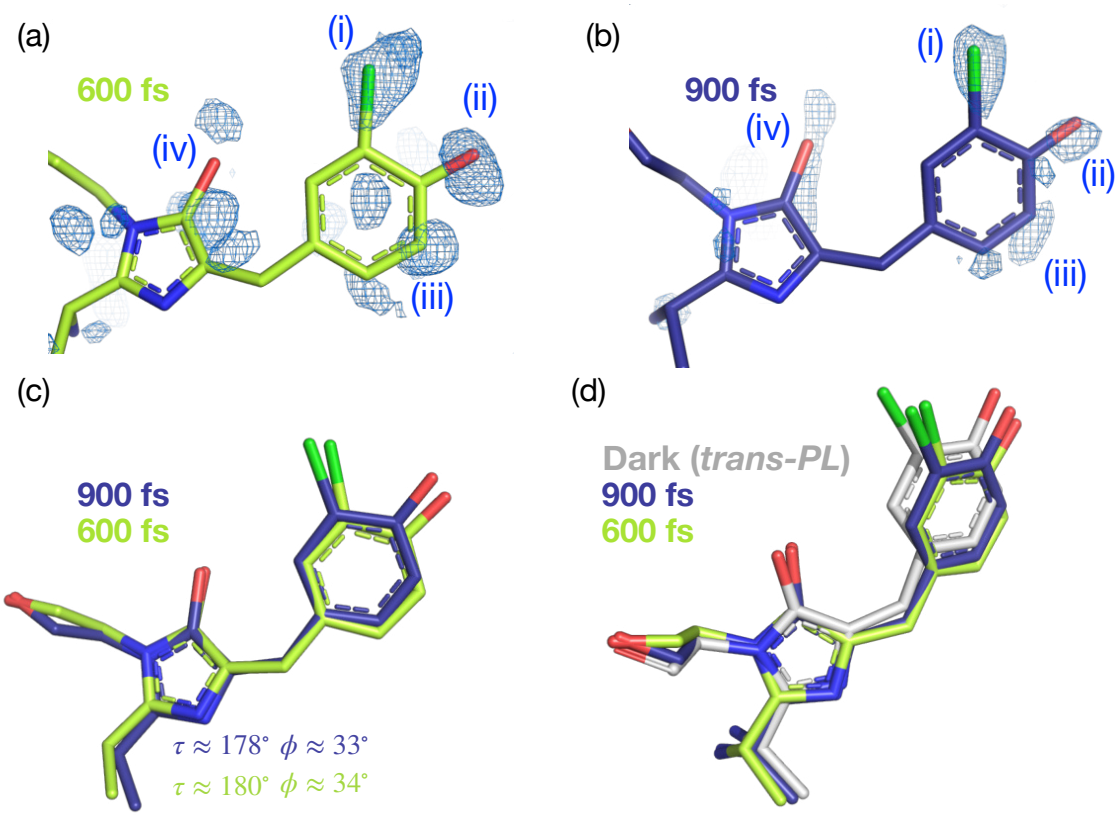

Figure S13. The WΔF_{max} maps for the **(a)** 600 fs and **(b)** 900 fs datasets are shown together at +2.1σ with the respective refined chromophore coordinates. The following four characteristics of these maps are marked: (i) the presence of Peak 1 (ii) a peak where the phenol ring oxygen is positioned by refinement (iii) electron density for two further carbons of the phenol ring (iv) features that suggest a tilt of the imidazolidone ring oxygen towards the phenol ring. **(c-d)** show the superposition of the two femtosecond refined structures, which we attribute to the intermediate *trans-FS*, and their relationship to the dark *trans-PL* configuration. Related to Figures 4 and 5.

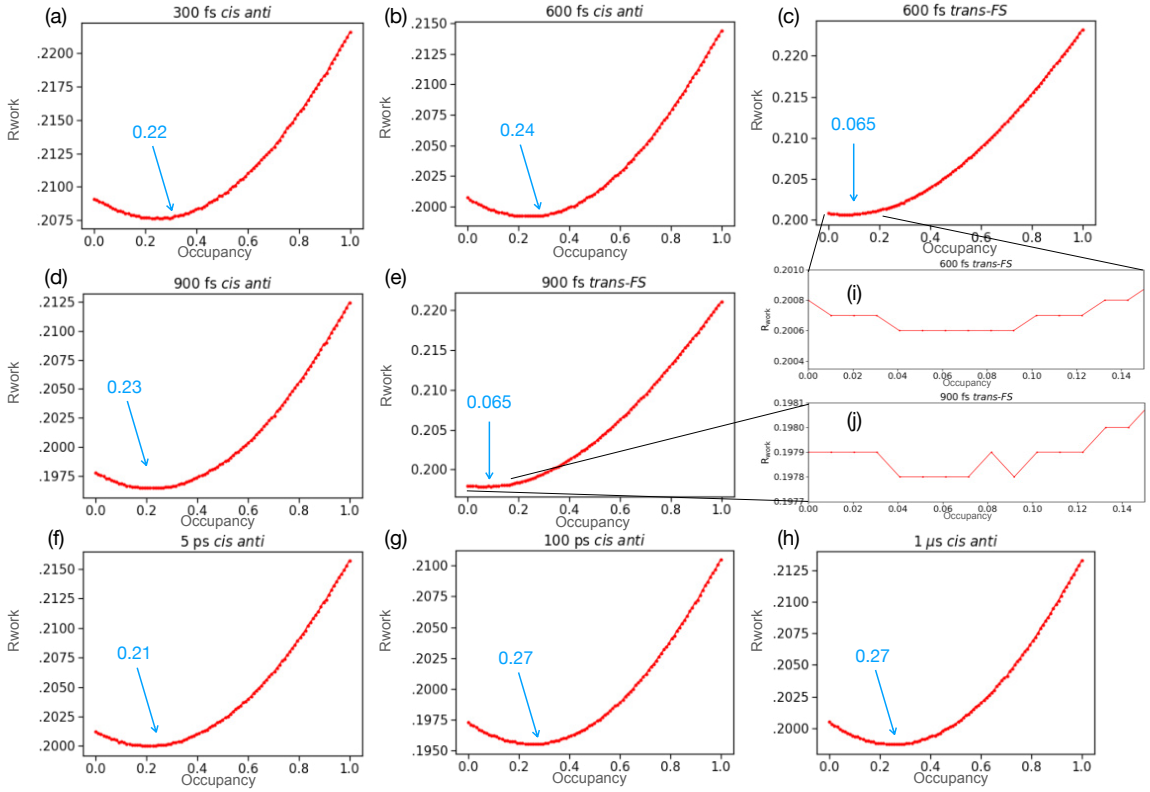

Figure S14. Occupancy refinement for light-induced chromophore conformations. These values were used to establish occupancies for the light coordinates (in order: PDBs 8A6N, 8A6O, 8A6P, 8A6Q, 8A6R, 8A6S). Related to Figure 4.

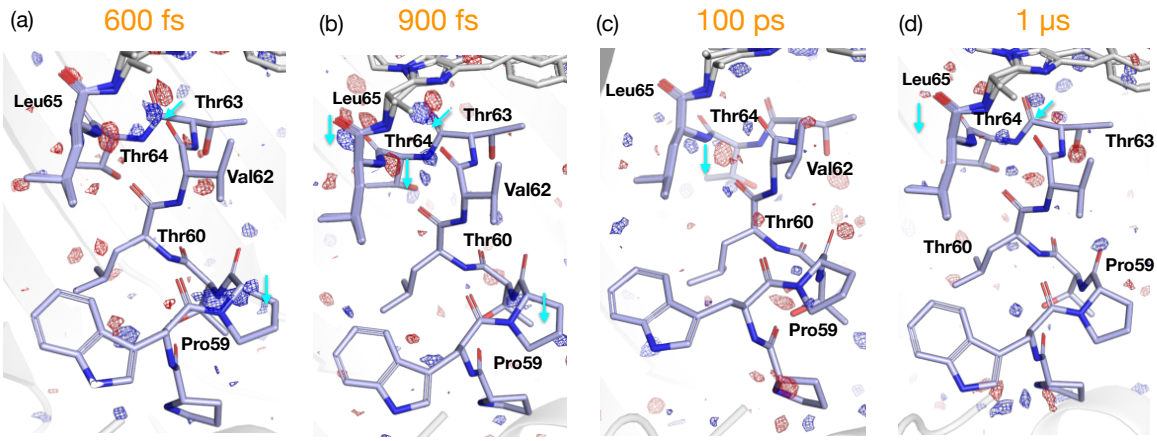

Figure S15. Difference electron density (DED) signals in the region of the central α-helix. WΔF_{max} maps are shown for each timepoint at +/-3σ (red=negative, blue=positive). The labeled residues present the most significant DED features and suggest an overall downward movement of the helix on a sub-picosecond timescale, which is particularly evident looking at residues Leu65, Thr63, and Pro59. Similar signals persist at the longer time points **(c-d)** but are weaker. Related to Figure 5.

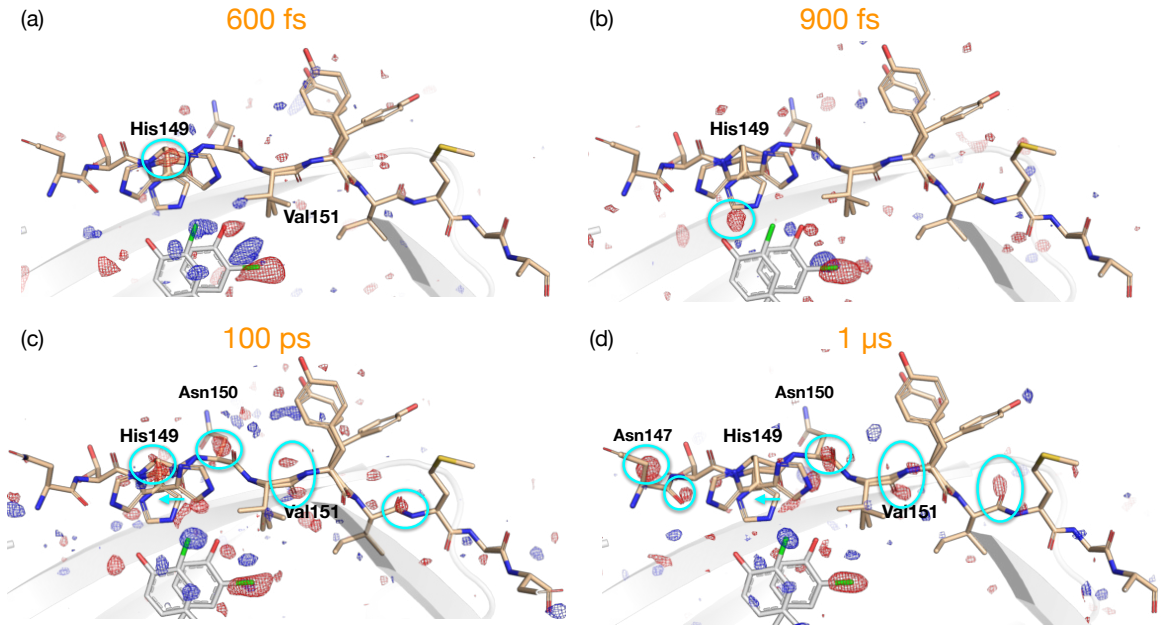

Figure S16. Difference electron density (DED) signals in the region of the β7 sheet. WΔF_{max} maps are shown for each timepoint at +/-3σ (red=negative, blue=positive). The femtosecond maps **(a-b)** have strong negative features on one of the His149 conformations. At 100 ps and 1 μs **(c-d)**, there are negative signals on the side chains and backbone of residues of Asn147, Asn150, and Val151. These are superimposable between the two datasets and suggest a downward movement of the *beta*-sheet away from the chromophore. The His149 flip that accompanies the *trans-to-cis* isomerization of the chromophore is marked by negative density on the *trans-PL*-associated conformation of this residue. Related to Figure 5.

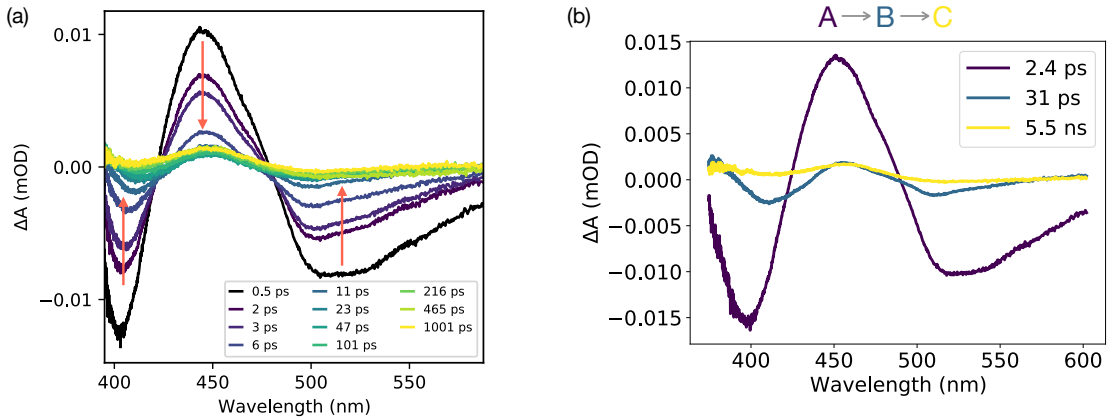

Figure S17. **(a)** Transient difference absorption spectra recorded at different pump-probe time delays after a femtosecond laser excitation (400 nm) starting from the rsEGFP2 (non-chlorinated) OFF state. **(b)** Components fitted through global analysis of the data shown in **(a)**, using a sequential model. Related to Figure 6.

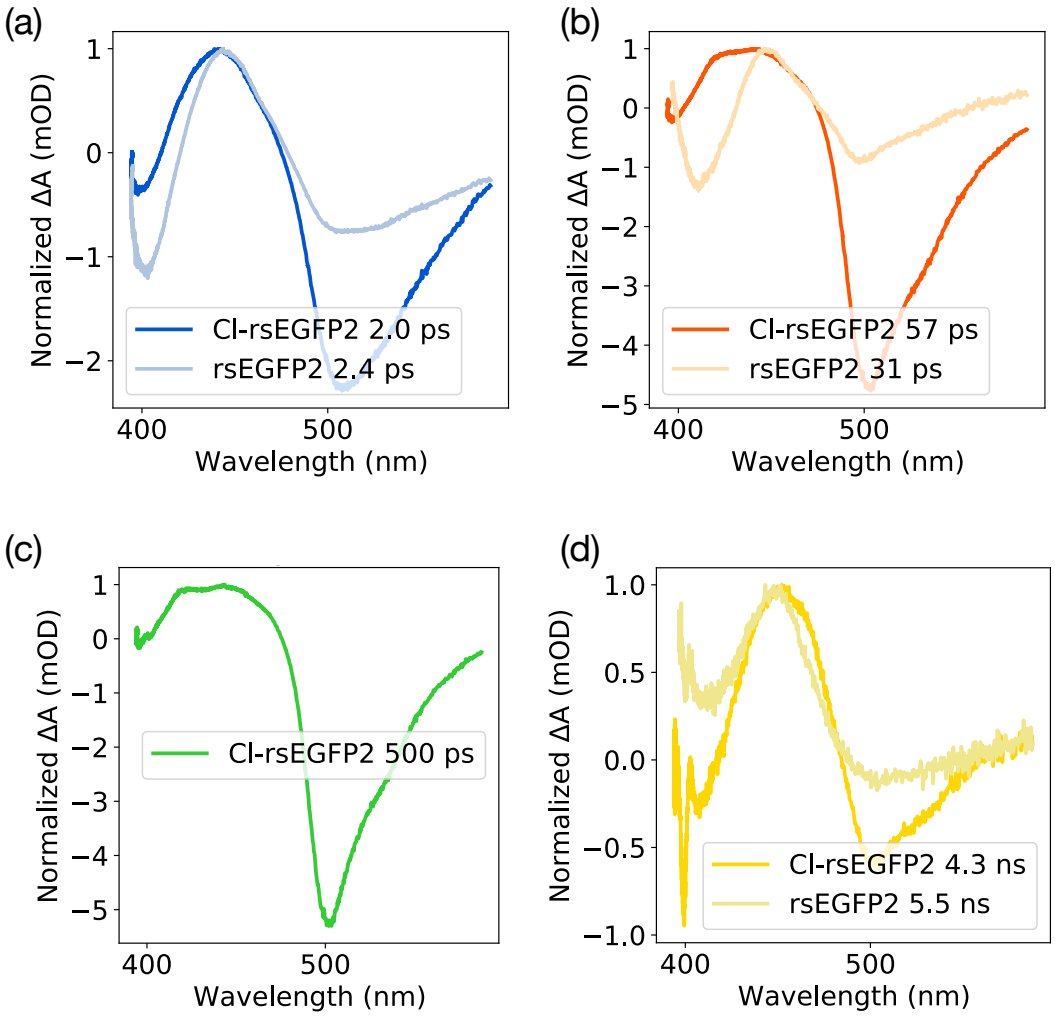

Figure S18. UV-Vis TA global analysis results comparison for rsEGFP2 (non-chlorinated) and Cl-rsEGFP2. Respective components are overlapped in **(a-d)**. Related to Figure 6.

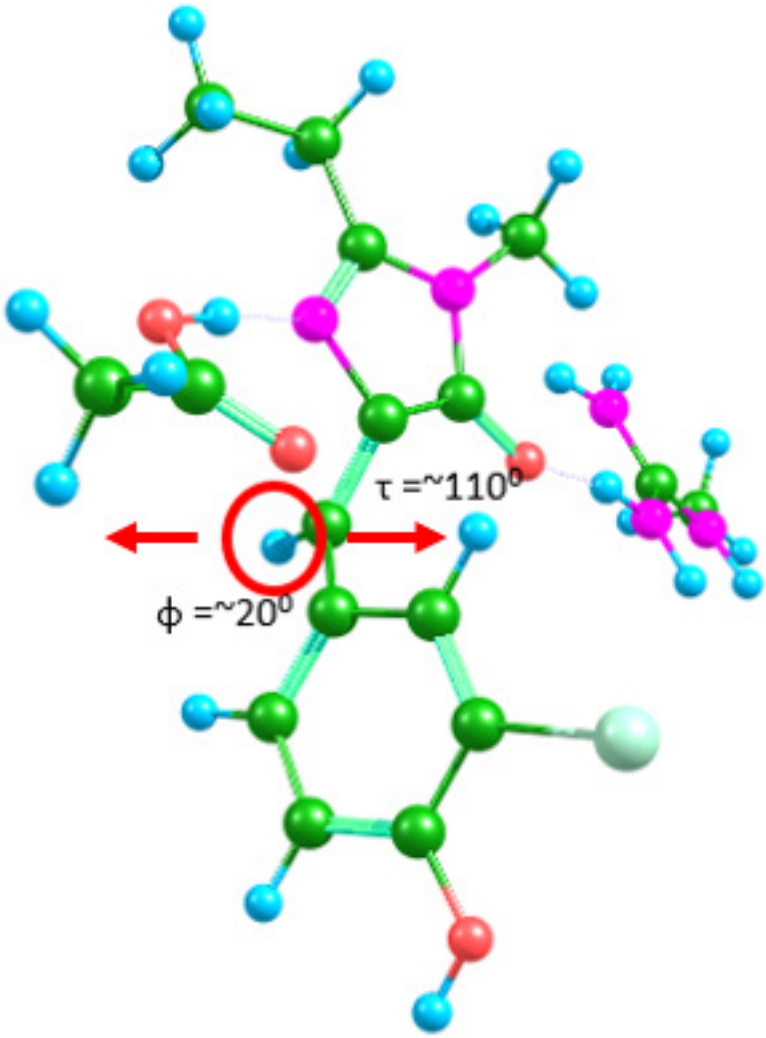

Figure S19. Geometry of the QM atoms at minimum energy conical intersection point (MECI) optimized with QM-MM. Red arrows indicate movement of the bridge hydrogen required to reach *trans* (left arrow) or *cis* (right arrow) isomers of the chromophore upon deactivation. Related to Figure 7.

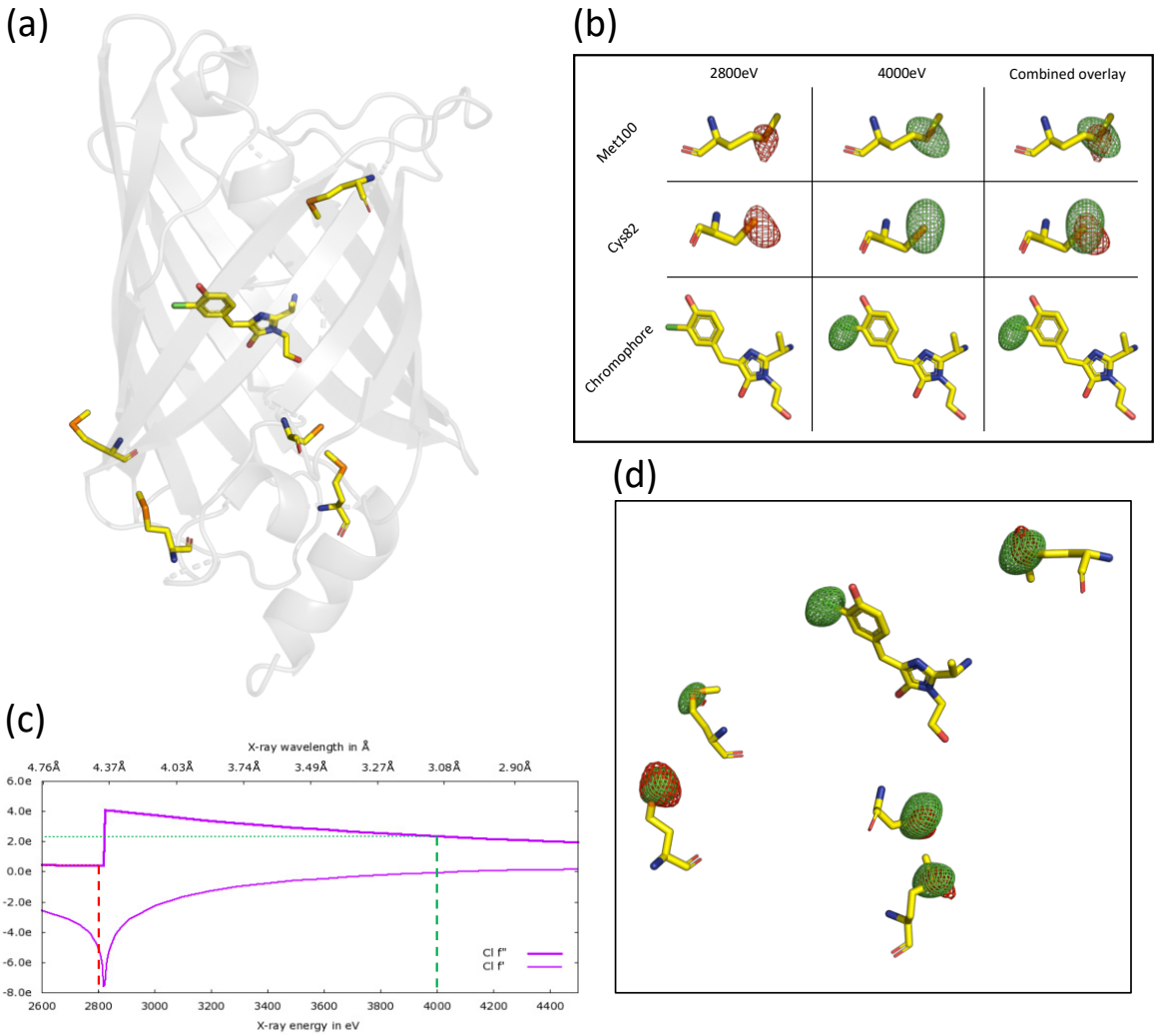

Figure S20. (a) Cartoon overview of Cl-rsEGFP2 with anomalous scatterer-containing residues and chromophore locations shown as sticks. **(b)** Anomalous difference Fourier maps for Met100, Cys82 and the chromophore above (4000 eV) and below (2800 eV) the chlorine K edge. Density presence in both maps indicates a sulphur atom, presence in the 4000 eV map combined with absence in the 2800 eV map confirms chlorine location. **(c)** f' and f" plot for Cl over the wavelength range used. Data collection wavelengths indicated as dashed lines, green for 4000eV above chlorine K edge, red for 2800 eV below. **(d)** Anomalous difference Fourier maps, both at 2800 eV and 4000 eV, for all scatterers in the structure shown with respective residues and chromophore. Related to Figure 3.

Name:	dark_CW-400nm-scale.hkl	neg5pe-400nm-scale.hkl	300fs-400nm-scale.hkl	600fs-400nm-scale.hkl	900fs-400nm-scale.hkl	5ps-400nm-scale.hkl	100ps-400nm-scale.hkl	1us-400nm-scale.hkl
Indexed Patterns:	56163	48496	18634	37132	37782	29251	55733	40977
Resolution Limits (Å):	31,46-1,80 (1,864-1,800) (1)	31,46-1,80 (1,864-1,800) (1)	31,46-1,80 (1,864-1,800) (1)	31,46-1,80 (1,864-1,800) (1)	31,46-1,80 (1,864-1,800) (1)	31,46-1,80 (1,864-1,800) (1)	31,46-1,80 (1,864-1,800) (1)	31,46-1,80 (1,864-1,800) (1)
	31,46-1,70 (1,761-1,700) (2)	31,46-1,70 (1,761-1,700) (2)	31,46-1,70 (1,761-1,700) (2)	31,46-1,70 (1,761-1,700) (2)	31,46-1,70 (1,761-1,700) (2)	31,46-1,70 (1,761-1,700) (2)	31,46-1,70 (1,761-1,700) (2)	31,46-1,70 (1,761-1,700) (2)
	31,46-1,60 (1,657-1,600) (3)	31,46-1,60 (1,657-1,600) (3)	31,46-1,60 (1,657-1,600) (3)	31,46-1,60 (1,657-1,600) (3)	31,46-1,60 (1,657-1,600) (3)	31,46-1,60 (1,657-1,600) (3)	31,46-1,60 (1,657-1,600) (3)	31,46-1,60 (1,657-1,600) (3)
No. Unique reflection Indices:	22565 (1)	22565 (1)	22565 (1)	22565 (1)	22565 (1)	22565 (1)	22565 (1)	22565 (1)
	26688 (2)	26688 (2)	26688 (2)	26688 (2)	26688 (2)	26688 (2)	26688 (2)	26688 (2)
	31903 (3)	31903 (3)	31903 (3)	31903 (3)	31903 (3)	31903 (3)	31903 (3)	31903 (3)
No. Merged Reflections:	16501938 (9322123) (1)	14362196 (812915) (1)	5563788 (311307) (1)	10768669 (599450) (1)	11443185 (642832) (1)	8984192 (518649) (1)	15876885 (886790) (1)	11405674 (620880) (1)
	17947205 (877345) (2)	15629890 (770468) (2)	6043619 (290868) (2)	11695184 (562109) (2)	12441190 (605769) (2)	9801052 (497179) (2)	17244054 (829337) (2)	12351835 (570486) (2)
	19272677 (7265017) (3)	16793655 (638406) (3)	6477970 (238031) (3)	12533266 (457868) (3)	13354810 (500733) (3)	10567486 (424206) (3)	18479758 (674892) (3)	13179653 (448944) (3)
Completeness (%):	100,00 (100,00) (1)	100,00 (100,00) (1)	100,00 (100,00) (1)	100,00 (100,00) (1)	100,00 (100,00) (1)	100,00 (100,00) (1)	100,00 (100,00) (1)	100,00 (100,00) (1)
	100,00 (100,00) (2)	100,00 (100,00) (2)	100,00 (100,00) (2)	100,00 (100,00) (2)	100,00 (100,00) (2)	100,00 (100,00) (2)	100,00 (100,00) (2)	100,00 (100,00) (2)
	100,00 (100,00) (3)	100,00 (100,00) (3)	100,00 (99,97) (3)	100,00 (100,00) (3)	100,00 (100,00) (3)	100,00 (100,00) (3)	100,00 (100,00) (3)	100,00 (100,00) (3)
Signal to noise:	9,007 (3,79) (1)	8,395 (3,54) (1)	5,239 (2,18) (1)	7,329 (3,08) (1)	7,442 (3,24) (1)	6,753 (3,05) (1)	9,080 (3,71) (1)	7,682 (3,11) (1)
	8,028 (2,44) (2)	7,481 (2,28) (2)	4,664 (1,38) (2)	6,526 (1,97) (2)	6,647 (2,11) (2)	6,048 (2,01) (2)	8,071 (2,32) (2)	6,821 (1,89) (2)
	6,973 (1,36) (3)	6,500 (1,30) (3)	4,052 (0,79) (3)	5,661 (1,08) (3)	5,787 (1,23) (3)	5,278 (1,21) (3)	6,987 (1,26) (3)	5,903 (1,04) (3)
Wilson b factor:	27,58 (1)	27,41 (1)	27,79 (1)	27,48 (1)	27,44 (1)	27,22 (1)	27,79 (1)	28,00 (1)
	29,27 (2)	29,23 (2)	29,57 (2)	29,25 (2)	29,12 (2)	28,93 (2)	29,57 (2)	29,82 (2)
	30,19 (3)	30,11 (3)	30,29 (3)	30,27 (3)	29,99 (3)	29,85 (3)	30,56 (3)	30,57 (3)
R_{split} (%):	8,89 (30,14) (1)	9,98 (32,17) (1)	15,55 (53,80) (1)	11,34 (37,64) (1)	10,64 (34,53) (1)	12,22 (36,28) (1)	8,71 (32,23) (1)	10,45 (37,26) (1)
	9,11 (51,23) (2)	10,21 (54,62) (2)	15,95 (94,06) (2)	11,62 (63,96) (2)	10,90 (60,53) (2)	12,49 (62,56) (2)	8,95 (54,93) (2)	10,72 (67,38) (2)
	9,40 (101,17) (3)	10,53 (106,51) (3)	16,50 (183,78) (3)	11,99 (132,67) (3)	11,26 (116,74) (3)	12,85 (120,72) (3)	9,26 (112,17) (3)	11,11 (139,69) (3)
CC*	1,00 (0,97) (1)	1,00 (0,97) (1)	0,99 (0,92) (1)	0,99 (0,96) (1)	1,00 (0,97) (1)	0,99 (0,96) (1)	1,00 (0,97) (1)	0,99 (0,96) (1)
	1,00 (0,94) (2)	1,00 (0,93) (2)	0,99 (0,84) (2)	0,99 (0,90) (2)	1,00 (0,92) (2)	0,99 (0,90) (2)	1,00 (0,93) (2)	0,99 (0,91) (2)
	1,00 (0,83) (3)	1,00 (0,81) (3)	0,99 (0,59) (3)	0,99 (0,74) (3)	1,00 (0,77) (3)	0,99 (0,77) (3)	1,00 (0,81) (3)	1,00 (0,74) (3)
$CC_{1/2}$	0,99 (0,90) (1)	0,98 (0,90) (1)	0,96 (0,74) (1)	0,98 (0,86) (1)	0,98 (0,88) (1)	0,98 (0,85) (1)	0,99 (0,89) (1)	0,98 (0,86) (1)
	0,99 (0,79) (2)	0,98 (0,76) (2)	0,96 (0,55) (2)	0,98 (0,69) (2)	0,98 (0,72) (2)	0,98 (0,69) (2)	0,99 (0,76) (2)	0,98 (0,71) (2)
	0,99 (0,52) (3)	0,98 (0,48) (3)	0,96 (0,21) (3)	0,98 (0,38) (3)	0,98 (0,43) (3)	0,98 (0,42) (3)	0,99 (0,48) (3)	0,98 (0,38) (3)

Table S1. CrystFEL merging statistics for the eight datasets collected, reported at three different high resolution cutoffs.

Dataset :	SACLA 2021 -5ps Cl-rsEGFP2	SACLA 2021 Interleaved Dark Cl-rsEGFP2	SACLA 2019 Interleaved Dark rsEGFP2	SSRL Cryo + Dehydrated Cl-rsEGFP2
Resolution range :	1.63 (1.688 - 1.63)	1.63 (1.688 - 1.63)	19.1 - 1.463 (1.515 - 1.46)	38.79 - 1.81 (1.875 - 1.81)
Space group :	P 21 21 21	P 21 21 21	P 21 21 21	P 21 21 21
Unit cell :	51.99 62.91 72.03 90 90 90	51.99 62.91 72.03 90 90 90	51.97 63.04 72.03 90 90 90	51.48 59.00 64.48 90 90 90
Reflections used in refinement :	30141 (2952)	30141 (2951)	36821 (340)	18407 (1804)
Reflections used for R-free :	1510 (146)	1510 (146)	1790 (19)	921 (91)
R-work :	0.1685 (0.3102)	0.1634 (0.2939)	0.1696 (0.4389)	0.2027 (0.3068)
R-free :	0.2013 (0.3369)	0.2000 (0.3428)	0.1952 (0.4783)	0.2266 (0.3376)
Number of non-hydrogen atoms :	2277	2277	2097	1906
macromolecules	2089	2089	1883	1756
ligands	63	63	40	41
solvent	125	125	174	109
Protein residues :	235	235	235	225
RMS(bonds) :	0.017	0.017	0.027	0.007
RMS(angles) :	1.46	1.46	1.78	0.93
Ramachandran favored (%) :	99.13	99.13	99.13	98.64
Ramachandran allowed (%) :	0.87	0.87	0.87	1.36
Ramachandran outliers (%) :	0	0	0	0
Rotamer outliers (%) :	2.09	2.09	1.9	0
Clashscore :	6.16	6.16	3.17	2.01
Average B-factor :	28.44	28.44	27.37	34.47
macromolecules	28.23	28.23	26.4	34.26
ligands	19.27	19.27	16.28	35.01
solvent	36.56	36.56	40.46	37.7

Table S2. Refinement statistics for: the refined dark model from the SACLA 2021 experiment computed using the interleaved dark (dark-CW) and negative 5 ps datasets, the refined dark model from the SACLA 2019 experiment, the SSRL cryo-dataset. Related to Figures 3-5.

Structure	Construct	Main *trans* Configuration	Method	Unit Cell (a b c – Å)
6PFT	Cl-rsEGFP2	*trans-TW* (*syn*)	irradiate -> cryocool	51.0 62.7 68.6
6PFU	Cl-rsEGFP2	*trans-PL* (*anti*)	dehydrate -> irradiate -> cryocool	51.3 59.5 65.4
8A83	Cl-rsEGFP2	*trans-PL* (*anti*)	irradiate -> dehydrate -> cryocool	51.5 59.0 64.5
8A6G	Cl-rsEGFP2	*trans-PL*	dark, room temperature SFX data	52.0 63.0 72.0
8A7V	rsEGFP2	*trans-TW*	dark, room temperature SFX data	52.0 63.0 72.0
7O7X	rsEGFP2 V151A	*trans-TW*	dark, room temperature SFX data	51.8 62.7 71.6
7O7W	rsEGFP2 V151L	*trans-PL*	dark, room temperature SFX data	51.8 62.9 71.9

Table S3. Summary table of unit cell dimensions for rsEGFP2 structures (chlorinated and non-) from this and other studies. Related to Figure 3.

Supporting Notes

1. OFF State SFX Structure for Cl-rsEGFP2

Our room temperature dark structure for Cl-rsEGFP2 presents predominantly the planar *trans anti* configuration (*trans-PL*) and minor populations of *trans syn* (*trans-TW*), and *cis anti* configurations (Figure S4). A previous cryotrapping crystallographic study[2] identified the *trans-PL* and *trans-TW* configurations as photoproducts of the HT and OBF pathways respectively. The *trans-PL* photoproduct was found in the structure with a contracted unit cell, while *trans-TW* was the primary configuration in the structure from the larger unit cell. This led to the conclusion that the choice of pathway is dependent on the crystal packing, where tighter packing favors the volume-conserving HT. Interestingly, our dark room temperature SFX structure presents mainly the *trans-PL* form, despite its large unit cell, when the chlorine substituent is present (Table S3 and Figure S5). This suggests that the *cis*-to-*trans* isomerization pathway at room temperature is a hula-twist, independent of unit cell dimensions. Table S3 lists the predominant conformations for the Cl-rsEGFP2 structures in this paper and in the cryotrapping study[2], with the corresponding treatments, as well as other published rsEGFP2 SFX structures. Room temperature SFX data indicate that the difference in chromophore conformation observed by Chang *et al.*[2] was induced by the dehydration protocol or the freezing process itself, rather than dictated by a lattice-dependent change in pathway. This interpretation is further supported by a separate cryotrapping experiment (row 3 of Table S3 and Figure S6, PDB 8A83) where the ON state crystal is first irradiated with 488 nm light, dehydrated into the smaller unit cell size, and then subsequently cryocooled; the resulting structure shows a *trans-PL* chromophore.

Supporting Procedures

1. 2021 SFX Data Analysis

1.1. Frame Data Processing and Crystallographic Analysis

A bad/damaged pixel mask for the detector was generated from dark scans recorded before data collection and was applied across all image data processing. Peak and hit finding were performed using Cheetah[3,4]. Identified hits were then indexed and integrated in CrystFEL[5,6] using the XGANDALF algorithm[7]. The achieved indexing rate was around 80% for all data. Indexed crystals from CrystFEL streamfiles were binned into different time delays and separated as "light" (pump laser on) and "dark" (pump laser off) to generate respective reflection files using a custom python script. Merging statistics for the datasets collected are reported in Table S1. The PHENIX[8] reflection conversion function was used to convert intensities to structure factors and model refinement was done using the phenix.refine function. Minor chromophore

populations in the dark structure were manually refined (PDB 8A6G). Low resolution (30 Å) and high resolution (1.63 Å) cutoffs were applied. Q-weighted difference electron density maps and background subtracted maps were then generated as explained in Section 2 of the Supporting Procedures.

For the analysis of protein-wide pump-induced changes, we used the scripts by Wickstrand *et al.*[9]. In short, a spherical volume of radius 2.0 Å was walked across every atom in the protein and the positive and negative difference electron densities from each dataset's Q-weighted map were averaged separately within each volume. A cut-off of +/-3σs and a grid spacing of 0.5 Å were used in the scripts.

1.2. Time Zero Determination by Cross Correlation

The cross-correlation of the optical and X-rays pulses was measured via the standard technique, previously described[10]. Briefly, a 50 μm thick, semi-conducting crystal (Ce:YAG) was placed in the interaction region. The transmission intensity of the optical pulse through the crystal was measured by a photo-diode. Exposure to hard X-rays causes modulation of the crystal's reflective and transmissive properties. The amplitude of the optical transmission was monitored while the temporal delay between the two pulses was scanned. With appropriate volume of data and averaging, the resulting signal exhibits a step-like function, centred approximately when the two pulse are overlapped in the temporal delay. The signal measured on the photo-diode (Figure S3(a)) as a function of delay was fitted as previously described[11]. The averaged time zero over a number of runs was used to correct the delay stage, to give an accurate time zero and, as such, an accurate binning for each data set (300 fs, 600 fs, 900 fs, 5 ps).

SACLA has recently implemented a feedback system between the optical and X-ray pulse, using a balanced optical-microwave phase detector (BOMPD)[12]. This corrects for long-term temporal drift over several hours or days which previously caused movement on the order of 60 - 100 fs[11]. The BOMPD feedback loop, additionally, reduces X-ray jitter stemming from an intrinsic instability in the Self Amplified Spontaneous Emission (SASE) process to sub 50 fs. Since it was difficult to suppress the actual timing drift using only a BOMPD, the drift here was further compensated using a phase shifter and the timing tool data. The jitter measured from the cross-correlation fittings is shown in (Figure S3(b)). As an additional precaution to mitigate drift, the cross-correlation was measured before the start of each day. Furthermore, the reflection intensity (transmission^{-1}) was measured and used as a comparative cross-correlation.

With the various steps taken described above, as-well as the new feedback system implemented at SACLA, we were able to accurately bin the data into sub picosecond bins (300, 600 and 900 fs) and confidently ascribe the ultrafast dynamics.

1.3. Generation of Q-weighted Maps

Through the *reciprocalspaceship* library[13], dark and light structure factors (F_{obs_D} and F_{obs_L} respectively) are in turn scaled to the structure factors calculated from the refined dark structure (F_{calc}).A simple scale factor *m* is applied to an entire dataset (Figure S7(a-b)). Q-weighted difference electron density maps are then calculated using weighted structure factor amplitudes, where the Bayesian weight applied is based on the work of Ursby *et al.*[14,15] and implemented in python using *reciprocalspaceship* (Figure S7(c-d)). A value of α = 0.2 is used here. Maps where the scaling is done using the SCALEIT program within the CCP4 suite[16] and the Q-weighting is implemented as in[17–19] present the same key features as those generated by the method described here (not shown). The easy implementation in python, however, allows for easy manipulation and visualization of the structure factor distributions and screening of improved map generation parameters (such as scale factor and α values).

1.4. Principal Component Analysis (PCA) of Electron Density Maps

Principal component analysis (PCA) of the Q-weighted maps described above is performed in python by loading each map as a NumPy array through the GEMMI library for structural biology (GEMMI version 0.4.5). A solvent mask and a mask that only retains grid points within 7 Å of the chromophore are applied. PCA is then sklearn.decomposition.PCA function (Scikit-learn version 1.0.1). Figure S8 presents the pipeline and results for PCA on the six DED maps. The first 5 components (C1-C5) are shown (noting that the

component sign is arbitrary in the analysis). PCA here is used primarily as a method to improve the data signal-to-noise ratio: the 6th component (C6) is identified as noise and the final difference maps shown in Figure 4 are reconstructed without it.

1.5. Generation of Background Subtracted Maps (WΔF_{max} maps)

In order to refine light-induced coordinates, one ideally wants to separate the signal that belongs to the photoproduct population from that of the dark state. Because only a small percentage of protein molecules actually undergo photoactivation, the problem of extracting the electron density of the photoproduct is a very similar issue to the one Pearce and colleagues describe of discerning minor states in macromolecular crystallography[1]. Pearce *et al.* generate background corrected maps by subtracting the "ground state" $2mF_o$-DF_c map from the "dataset" $2mF_o$-DF_c map as follows :

$$[\text{corrected map}] = [\text{dataset map}] - N_{bg} \times [\text{ground state map}] \quad (1)$$

where the background correction factor (we refer to it here as N_{bg}, in[1] it is called BDC – Background Density Correction factor) is the value that maximizes the difference in correlation (calculated from the ground state and the corrected map) between the entire protein and a specific area of change.
We have extended this here to Q-weighted maps. Figure S9 describes the steps involved in generating what we have called WΔF_{max} maps. Q-weighted maps of the form :

$$W\Delta F_{corr} = w \times (\mid F_{obs_L} \mid - N_{bg} \times \mid F_{obs_D} \mid) \quad (2)$$

are generated for a range of N_{bg} between 0 and 1 and saved as electron density maps in CCP4 format. In real space, a local region, R_{loc}, is defined as a sphere of 5 Å centered around the chromophore double bond. The entire protein is defined as R_{glob} after a solvent mask is applied. For each value of N_{bg}, we compute the Pearson correlation coefficient between the respective $W\Delta F_{corr}$ map and the map obtained from the dark model calculated structure factors (F_{calc}). This is done for both R_{loc} and R_{glob}. We then choose the N_{bg} value that maximizes the difference between these two correlation coefficients and save the corresponding map (WΔF_{max}) for that timepoint. The determination of the appropriate background subtraction value for each timepoint is shown in Figure S10 and the corresponding WΔF_{max} maps are shown in Figure S11. The *cis anti* photoproduct is discernible already at 300 fs and is very clear in the 100 ps and 1 μs maps. The maps from the 600 fs and 900 fs datasets contain additional features (numbered (i-iv)) that support the presence of the femtosecond intermediate *trans-FS* (see main text and Figure S13). The 5 ps WΔF_{max} map, just as the respective Q-weighted map, is noisier than the other datasets, though it still contains weak *trans-FS* features and some *cis anti* population. Figure S12 displays background corrected maps generated by subtraction of light and dark $2mF_o$-DF_c as done in[1]. These are very similar to the ones calculated directly from reciprocal space and support the conclusions drawn above.

Refinement of Cl-rsEGFP2 coordinates to WΔF_{max} maps is done, starting from the dark coordinates, with phenix.refine by allowing only atom positions from the chromophore and the residues immediately next to it in the sequence (residues 63-65 and 69-71) to vary. This is because the background subtracted structure factors are much lower signal-to-noise than the ones used to refine the dark structure, and we therefore limit their use to the chromophore region where light-induced changes are strong enough to clearly reveal the presence of minor populations. Occupancies for the *cis anti* and *trans-FS* species in light datasets were refined so as to minimize R_{work} (Figure S14). Despite the weak presence of *trans-FS* features in the 5 ps maps, *trans-FS* occupancy refinement (not shown) for this timepoint did not yield a significant population, so this conformation was not included in the final coordinates. Final structures for each time point are deposited (in order from 300 fs to 1 μs) as PDBs 8A6N, 8A6O, 8A6P, 8A6Q, 8A6R, 8A6S.

2. 2019 SFX for OFF-state rsEGFP2 structure

Dark data was collected at SACLA at the BL3 EH2 beamline with setup equivalent to the one described above (MPCCD-phase III detector, 10.5 keV), but a refined detector distance of 50.6 mm. Data was then

processed as described for the 2021 SFX experiment, with the difference that structure refinement was done in REFMAC[20] (PDB 8A7V).

3. Extra-Cryotrapping Experiment

Crystals were grown as described in[2]. For the irradiation/dehydration protocol, the crystal was fished onto a loop and transferred to a separate droplet of mother liquor on a cover slip. The entire cover slip was picked up with tweezers and placed in the beam of a 488nm laser (specifics as in[2]). Illumination lasted between 20-30 seconds. Following this, the crystal was transferred to a drop of dehydrating cryoprotectant[2] and placed long enough to contract into the smaller unit cell size (approximately 5 seconds). It was then fished out onto a loop again and plunged into liquid nitrogen. Data was collected at the SSRL 7-1 beamline. Data reduction and refinement were then done using XDS[21] and Phenix[8] (PDB 8A83).Refinement statistics for this cryotrapped structure and for the dark structures collected at SACLA are reported in Table S2.

4. Quantum Chemical Modeling Details

QM-MM simulations in the protein were performed using our own version of GROMACS 4.6.5[22,23] coupled to the Terachem[24,25] (for ground state) and GAMESS(US)[26] (for excited-state) quantum chemistry packages. We searched for minimum-energy geometries in all systems using the limited-memory Broyden-Fletcher-Goldfard-Shannon (L-BFGS) quasi-Newton optimization algorithm, without PBC and with infinite cut-offs for the Coulomb and Lennard-Jones interactions. All optimizations in the work were performed until the maximum component of the force was lower than 10 kJ/mol/nm. Vertical absorption and emission spectra calculations were performed with xMCQDPT2 method implemented in the Firefly package[27].

4.1. Planar Ground and Excited State trans-PL Structures

Initially, we performed optimization of the Cl-rsEGFP2 on ground and excited states, starting from the dark *trans-PL* crystal structure. On the ground state, we performed optimization with density functional theory (DFT) at PBE0/cc-pVDZ//Amber03[28–30] with empirical corrections to dispersion energies and interactions introduced with Grimme's DFT-D3 model[31]. On the excited state, a double optimization scheme was employed. At first, SA2-CASSCF(2,2)/3-21G//Amber03[32] was used to minimize the S1 state. We used a small active space in this optimization to prevent the interchange between the S1 and S2 states, which typically happens for the neutral GFP chromophores when using using larger active spaces without electron correlation. The structure optimised with the small active space, was subject to a second optimisation at the SA2-CASSCF(12,11)/3-21G//Amber03 level of theory.

Both S0 and S1 optimized structures are planar. Next, we computed vertical excitation and emission energies at the xMCQDPT2/SA6-CASSCF(12,11)/cc-pVDZ//Amber03 level of theory. All 6 states were included into averaging as well as into the effective Hamiltonian. Results suggest absorption at 405 nm (3.06 eV) and emission at 518 nm (2.39 eV). In addition for the S1 minimum energy geometry, we computed an excited-state absorption (ESA) from the S1 into the S5 of 425 nm (2.92 eV). These excitation energies are in line with the experimental data (Figure 6), and hence suggest that the model provides an adequate qualitative description for our system.

4.2. Identification of the Photoisomerization Pathway

At first, we performed a search for the isomerization pathway connected to the TR-SFX-resolved *trans-FS* structure at 900 fs. Optimization on the ground (PBE0/cc-pVDZ//Amber03) and excited (SA2-CASSCF(12,11)/3-21G//Amber03) states resulted in the planar *trans-PL* structure, suggesting that this twisted structure is not connected to any minima on the excited state. To identify minimum energy conical intersection points(MECI), we implemented a penalty function MECI search algorithm[33] with α=0.02 and σ=16 as the parameters for the penalty function. When starting the optimization from the the *trans-FS* structure, no MECI could be located, in line with previous computational studies[34,35] that suggest that in the neutral GFP-chromophores there is no conical intersection associated with the rotation of the phenol ring.

We next searched for a hula-twist MECI by manually increasing τ torsion angle by 45° in the *trans-FS* structure and optimising its geometry at the SA2-CASSCF(12,11)/3-21G//Amber03 level of theory. This optimisation resulted in a twisted structure with an S1/S0 energy gap of ≈0.035 a.u. Starting a MECI optimization from this geometry leads to the MECI structure shown in Figure S19 with an S1/S0 energy gap of ≈0.0005 a.u. After the optimizations we also recomputed energies for both twisted minima and MECI points with xMCQDPT2/SA6-CASSCF(12,11)/cc-pVDZ//Amber03. In addition, to determine whether the MECI point connects the anti-trans conformer to the anti-cis conformer, we performed a ground state optimisation at PBE0/cc-pVDZ//Amber03 level starting from the MECI. While a direct optimization leads to the original planar *anti-trans-PL* chromophore conformer, a slight perturbation of the position of the methylene hydrogen atom by ≈ 0.3 Å towards a more *cis*-like position, leads to the *anti-cis* conformer.

5. Confirming the Presence of the Chlorine Substituent

To confirm incorporation of the chlorine substituent into the chromophore, we analyzed anomalous difference Fourier maps from anomalous data taken at different wavelengths. Single crystals were obtained by the hanging-drop vapor diffusion method at 20 °C described previously[36]. Briefly, the protein solution (12 mg/mL, 50mM Hepes pH 7.5, 20 mM NaCl) was mixed 1:1 with the precipitant solution (100 mM Hepes pH 8.0, 1.80 M ammonium sulphate, 20 mM NaCl) to yield 2-4 muL drops that were placed over a well containing 1 mL of the precipitant solution. Mature crystals with dimensions up to 500 muLm x 200 muLm x 200 muLm appeared after three weeks. Prior to flash-freezing in liquid nitrogen, crystals were cryoprotected by passage through three solutions of incrementally increasing amounts of sucrose to a final concentration of 1.2M in 75 mM Hepes pH 8.1, 20 mM NaCl, 0.9 M ammonium sulphate.

Data was collected on beamline I23, Diamond Light Source, using the Pilatus 12M semi-cylindrical detector at a temperature of 50K[37]. Data were collected above and below the chlorine K absorption edge at 4.0 keV (λ=3.1 Å) and 2.8 keV (λ=4.4Å) respectively. Each dataset consisted of 3600 images at 0.1^{c}irc oscillation with 0.1s exposure. 3 x 360^{c}irc datasets at 4.0 keV were used to phase the structure using CRANK2. Further structure refinement was performed in Phenix and Coot (PDB 8AM4). Anomalous difference Fourier maps were generated using ANODE[38]. Figure S20 shows the resulting anomalous difference Fourier maps from 4.0 keV and 2.8 keV. The presence of density in the 4.0 keV dataset (green mesh, 5σ) in conjunction with the absence of density in the 2.8 keV dataset (red mesh, 4σ) is conclusive of Cl, confirming the identity of the chromophore heavy atom substitution.

6. OFF-to-ON Quantum Yield for the Cl-rsEGFP2 construct

We carried out a comparative measurement to estimate the reaction quantum yield (QY) for our chlorinated rsEGFP2 construct. The OFF-to-ON QY for unchlorinated rsEGFP2 was most recently estimated to 0.23[39]. rsEGFP2 and Cl-rsEGFP2 solutions were fully converted to the OFF state using through illumination with a 488 nm LED. The final OD at 405 nm for both was ≈ 0.25. The OFF-to-ON conversion was then driven with a 405 nm LED at 4.4 mW power and the absorption at 488 nm and 405 nm monitored with an Agilent 8453 spectrophotometer.

Triplicate measurements were averaged and normalized. Figure S1 shows the 405 nm absorption decay for both constructs with the respective fitted decay rates (k). From the ratio of the two fitted rates we estimate the OFF-to-ON QY for Cl-rsEGFP2:

$$\phi_{Cl} = \phi_{noCl} \times \frac{k_{Cl}}{k_{noCl}} = 0.2 \tag{3}$$

Supporting References

1. Pearce, N.M.; Krojer, T.; Bradley, A.R.; Collins, P.; Nowak, R.P.; Talon, R.; Marsden, B.D.; Kelm, S.; Shi, J.; Deane, C.M.; von Delft, F. A multi-crystal method for extracting obscured crystallographic states from conventionally uninterpretable electron density. *Nature Communications* **2017**, *8*, 15123. doi:10.1038/ncomms15123.
2. Chang, J.; Romei, M.G.; Boxer, S.G. Structural Evidence of Photoisomerization Pathways in Fluorescent Proteins. *Journal of the American Chemical Society* **2019**, *141*, 15504–15508. doi:10.1021/jacs.9b08356.
3. Barty, A.; Kirian, R.A.; Maia, F.R.N.C.; Hantke, M.; Yoon, C.H.; White, T.A.; Chapman, H. Cheetah : software for high-throughput reduction and analysis of serial femtosecond X-ray diffraction data. *Journal of Applied Crystallography* **2014**, *47*, 1118–1131. doi:10.1107/S1600576714007626.
4. Nakane, T.; Joti, Y.; Tono, K.; Yabashi, M.; Nango, E.; Iwata, S.; Ishitani, R.; Nureki, O. Data processing pipeline for serial femtosecond crystallography at SACLA. *Journal of Applied Crystallography* **2016**, *49*, 1035–1041. doi:10.1107/S1600576716005720.
5. White, T.A.; Kirian, R.A.; Martin, A.V.; Aquila, A.; Nass, K.; Barty, A.; Chapman, H.N. CrystFEL : a software suite for snapshot serial crystallography. *J. Appl. Cryst* **2012**, *45*, 335–341. doi:10.1107/S0021889812002312.
6. White, T.A.; Mariani, V.; Brehm, W.; Yefanov, O.; Barty, A.; Beyerlein, K.R.; Chervinskii, F.; Galli, L.; Gati, C.; Nakane, T.; Tolstikova, A.; Yamashita, K.; Yoon, C.H.; Diederichs, K.; Chapman, H.N. Recent developments in CrystFEL. *Journal of Applied Crystallography* **2016**, *49*, 680–689. doi:10.1107/S1600576716004751.
7. Gevorkov, Y.; Yefanov, O.; Barty, A.; White, T.A.; Mariani, V.; Brehm, W.; Tolstikova, A.; Grigat, R.R.; Chapman, H.N. XGANDALF – extended gradient descent algorithm for lattice finding. *Acta Crystallographica Section A Foundations and Advances* **2019**, *75*, 694–704. doi:10.1107/S2053273319010593.
8. Adams, P.D.; Afonine, P.V.; Bunkóczi, G.; Chen, V.B.; Davis, I.W.; Echols, N.; Headd, J.J.; Hung, L.W.; Kapral, G.J.; Grosse-Kunstleve, R.W.; McCoy, A.J.; Moriarty, N.W.; Oeffner, R.; Read, R.J.; Richardson, D.C.; Richardson, J.S.; Terwilliger, T.C.; Zwart, P.H.; IUCr. PHENIX: a comprehensive Python-based system for macromolecular structure solution. *Acta Crystallographica Section D Biological Crystallography* **2010**, *66*, 213–221. doi:10.1107/S0907444909052925.
9. Wickstrand, C.; Katona, G.; Nakane, T.; Nogly, P.; Standfuss, J.; Nango, E.; Neutze, R. A tool for visualizing protein motions in time-resolved crystallography. *Structural Dynamics* **2020**, *7*, 024701. doi:10.1063/1.5126921.
10. Gahl, C.; Azima, A.; Beye, M.; Deppe, M.; Döbrich, K.; Hasslinger, U.; Hennies, F.; Melnikov, A.; Nagasono, M.; Pietzsch, A.; Wolf, M.; Wurth, W.; Föhlisch, A. A femtosecond X-ray/optical cross-correlator. *Nature Photonics* **2008**, *2*, 165–169. doi:10.1038/nphoton.2007.298.
11. Sanchez-Gonzalez, A.; Johnson, A.S.; Fitzpatrick, A.; Hutchison, C.D.M.; Fare, C.; Cordon-Preciado, V.; Dorlhiac, G.; Ferreira, J.L.; Morgan, R.M.; Marangos, J.P.; Owada, S.; Nakane, T.; Tanaka, R.; Tono, K.; Iwata, S.; van Thor, J.J. Coincidence timing of femtosecond optical pulses in an X-ray free electron laser. *Journal of Applied Physics* **2017**, *122*, 203105. doi:10.1063/1.5012749.
12. Togashi, T.; Owada, S.; Kubota, Y.; Sueda, K.; Katayama, T.; Tomizawa, H.; Yabuuchi, T.; Tono, K.; Yabashi, M. Femtosecond Optical Laser System with Spatiotemporal Stabilization for Pump-Probe Experiments at SACLA. *Applied Sciences* **2020**, *10*, 7934. doi:10.3390/app10217934.
13. Greisman, J.B.; Dalton, K.M.; Hekstra, D.R. reciprocalspaceship : a Python library for crystallographic data analysis. *Journal of Applied Crystallography* **2021**, *54*, 1521–1529. doi:10.1107/S160057672100755X.
14. Terwilliger, T.C.; Berendzen, J. Bayesian Difference Refinement. *Acta Crystallographica Section D Biological Crystallography* **1996**, *52*, 1004–1011. doi:10.1107/S0907444996006725.
15. Ursby, T.; Bourgeois, D. Improved Estimation of Structure-Factor Difference Amplitudesfrom Poorly Accurate Data. *Acta Crystallographica Section A Foundations of Crystallography* **1997**, *53*, 564–575. doi:10.1107/S0108767397004522.
16. Winn, M.D.; Ballard, C.C.; Cowtan, K.D.; Dodson, E.J.; Emsley, P.; Evans, P.R.; Keegan, R.M.; Krissinel, E.B.; Leslie, A.G.W.; McCoy, A.; McNicholas, S.J.; Murshudov, G.N.; Pannu, N.S.; Potterton, E.A.; Powell, H.R.; Read, R.J.; Vagin, A.; Wilson, K.S. Overview of the CCP 4 suite and current developments. *Acta Crystallographica Section D Biological Crystallography* **2011**, *67*, 235–242. doi:10.1107/S0907444910045749.
17. Ren, Z.; Perman, B.; Šrajer, V.; Teng, T.Y.; Pradervand, C.; Bourgeois, D.; Schotte, F.; Ursby, T.; Kort, R.; Wulff, M.; Moffat, K. A Molecular Movie at 1.8 Å Resolution Displays the Photocycle of Photoactive Yellow Protein,

a Eubacterial Blue-Light Receptor, from Nanoseconds to Seconds †. *Biochemistry* **2001**, *40*, 13788–13801. doi:10.1021/bi0107142.

18. Schmidt, M.; Rajagopal, S.; Ren, Z.; Moffat yz, K. Application of Singular Value Decomposition to the Analysis of Time-Resolved Macromolecular X-Ray Data. *Biophysical Journal* **2002**, *84*, 2112–2129.
19. Pandey, S.; Bean, R.; Sato, T.; Poudyal, I.; Bielecki, J.; Cruz Villarreal, J.; Yefanov, O.; Mariani, V.; White, T.A.; Kupitz, C.; Hunter, M.; Abdellatif, M.H.; Bajt, S.; Bondar, V.; Echelmeier, A.; Doppler, D.; Emons, M.; Frank, M.; Fromme, R.; Gevorkov, Y.; Giovanetti, G.; Jiang, M.; Kim, D.; Kim, Y.; Kirkwood, H.; Klimovskaia, A.; Knoska, J.; Koua, F.H.M.; Letrun, R.; Lisova, S.; Maia, L.; Mazalova, V.; Meza, D.; Michelat, T.; Ourmazd, A.; Palmer, G.; Ramilli, M.; Schubert, R.; Schwander, P.; Silenzi, A.; Sztuk-Dambietz, J.; Tolstikova, A.; Chapman, H.N.; Ros, A.; Barty, A.; Fromme, P.; Mancuso, A.P.; Schmidt, M. Time-resolved serial femtosecond crystallography at the European XFEL. *Nature Methods* **2020**, *17*, 73–78. doi:10.1038/s41592-019-0628-z.
20. Murshudov, G.N.; Skubák, P.; Lebedev, A.A.; Pannu, N.S.; Steiner, R.A.; Nicholls, R.A.; Winn, M.D.; Long, F.; Vagin, A.A. REFMAC5 for the refinement of macromolecular crystal structures. *Acta crystallographica. Section D, Biological crystallography* **2011**, *67*, 355–67. doi:10.1107/S0907444911001314.
21. Kabsch, W. XDS. *Acta crystallographica. Section D, Biological crystallography* **2010**, *66*, 125–32. doi:10.1107/S0907444909047337.
22. Pronk, S.; Páll, S.; Schulz, R.; Larsson, P.; Bjelkmar, P.; Apostolov, R.; Shirts, M.R.; Smith, J.C.; Kasson, P.M.; van der Spoel, D.; Hess, B.; Lindahl, E. GROMACS 4.5: a high-throughput and highly parallel open source molecular simulation toolkit. *Bioinformatics* **2013**, *29*, 845–854. doi:10.1093/bioinformatics/btt055.
23. Morozov, D. Modified GROMACS 4.6.5 **2022**. doi:10.5281/ZENODO.6669552.
24. Titov, A.V.; Ufimtsev, I.S.; Luehr, N.; Martinez, T.J. Generating Efficient Quantum Chemistry Codes for Novel Architectures. *Journal of Chemical Theory and Computation* **2013**, *9*, 213–221. doi:10.1021/ct300321a.
25. Ufimtsev, I.S.; Martinez, T.J. Quantum Chemistry on Graphical Processing Units. 3. Analytical Energy Gradients, Geometry Optimization, and First Principles Molecular Dynamics. *Journal of Chemical Theory and Computation* **2009**, *5*, 2619–2628. doi:10.1021/ct9003004.
26. Barca, G.M.J.; Bertoni, C.; Carrington, L.; Datta, D.; De Silva, N.; Deustua, J.E.; Fedorov, D.G.; Gour, J.R.; Gunina, A.O.; Guidez, E.; Harville, T.; Irle, S.; Ivanic, J.; Kowalski, K.; Leang, S.S.; Li, H.; Li, W.; Lutz, J.J.; Magoulas, I.; Mato, J.; Mironov, V.; Nakata, H.; Pham, B.Q.; Piecuch, P.; Poole, D.; Pruitt, S.R.; Rendell, A.P.; Roskop, L.B.; Ruedenberg, K.; Sattasathuchana, T.; Schmidt, M.W.; Shen, J.; Slipchenko, L.; Sosonkina, M.; Sundriyal, V.; Tiwari, A.; Galvez Vallejo, J.L.; Westheimer, B.; Włoch, M.; Xu, P.; Zahariev, F.; Gordon, M.S. Recent developments in the general atomic and molecular electronic structure system. *The Journal of Chemical Physics* **2020**, *152*, 154102. doi:10.1063/5.0005188.
27. Granovsky, A.A. Extended multi-configuration quasi-degenerate perturbation theory: The new approach to multi-state multi-reference perturbation theory. *The Journal of Chemical Physics* **2011**, *134*, 214113. doi:10.1063/1.3596699.
28. Dunning, T.H. Gaussian basis sets for use in correlated molecular calculations. I. The atoms boron through neon and hydrogen. *The Journal of Chemical Physics* **1989**, *90*, 1007–1023. doi:10.1063/1.456153.
29. Duan, Y.; Wu, C.; Chowdhury, S.; Lee, M.C.; Xiong, G.; Zhang, W.; Yang, R.; Cieplak, P.; Luo, R.; Lee, T.; Caldwell, J.; Wang, J.; Kollman, P. A point-charge force field for molecular mechanics simulations of proteins based on condensed-phase quantum mechanical calculations. *Journal of Computational Chemistry* **2003**, *24*, 1999–2012. doi:10.1002/jcc.10349.
30. Adamo, C.; Barone, V. Toward reliable density functional methods without adjustable parameters: The PBE0 model. *The Journal of Chemical Physics* **1999**, *110*, 6158–6170. doi:10.1063/1.478522.
31. Grimme, S.; Antony, J.; Ehrlich, S.; Krieg, H. A consistent and accurate ab initio parametrization of density functional dispersion correction (DFT-D) for the 94 elements H-Pu. *The Journal of Chemical Physics* **2010**, *132*, 154104. doi:10.1063/1.3382344.
32. Siegbahn, P.E.M.; Almlöf, J.; Heiberg, A.; Roos, B.O. The complete active space SCF (CASSCF) method in a Newton–Raphson formulation with application to the HNO molecule. *The Journal of Chemical Physics* **1981**, *74*, 2384–2396. doi:10.1063/1.441359.
33. Levine, B.G.; Coe, J.D.; Martínez, T.J. Optimizing Conical Intersections without Derivative Coupling Vectors: Application to Multistate Multireference Second-Order Perturbation Theory (MS-CASPT2). *The Journal of Physical Chemistry B* **2008**, *112*, 405–413. doi:10.1021/jp0761618.

34. Polyakov, I.V.; Grigorenko, B.L.; Epifanovsky, E.M.; Krylov, A.I.; Nemukhin, A.V. Potential Energy Landscape of the Electronic States of the GFP Chromophore in Different Protonation Forms: Electronic Transition Energies and Conical Intersections. *Journal of Chemical Theory and Computation* **2010**, *6*, 2377–2387. doi:10.1021/ct100227k.
35. Weber, W.; Helms, V.; McCammon, J.A.; Langhoff, P.W. Shedding light on the dark and weakly fluorescent states of green fluorescent proteins. *Proceedings of the National Academy of Sciences* **1999**, *96*, 6177–6182. doi:10.1073/pnas.96.11.6177.
36. El Khatib, M.; Martins, A.; Bourgeois, D.; Colletier, J.P.; Adam, V. Rational design of ultrastable and reversibly photoswitchable fluorescent proteins for super-resolution imaging of the bacterial periplasm. *Scientific Reports* **2016**, *6*, 18459. doi:10.1038/srep18459.
37. Wagner, A.; Duman, R.; Henderson, K.; Mykhaylyk, V. In-vacuum long-wavelength macromolecular crystallography. *Acta Crystallographica Section D Structural Biology* **2016**, *72*, 430–439. doi:10.1107/S2059798316001078.
38. Thorn, A.; Sheldrick, G.M. ANODE : anomalous and heavy-atom density calculation. *Journal of Applied Crystallography* **2011**, *44*, 1285–1287. doi:10.1107/S0021889811041768.
39. Adam, V.; Hadjidemetriou, K.; Jensen, N.; Shoeman, R.L.; Woodhouse, J.; Aquila, A.; Banneville, A.S.; Barends, T.R.M.; Bezchastnov, V.; Boutet, S.; Byrdin, M.; Cammarata, M.; Carbajo, S.; Christou, N.E.; Coquelle, N.; Mora, E.D.l.; Khatib, M.E.; Chicano, T.M.; Doak, R.B.; Fieschi, F.; Foucar, L.; Glushonkov, O.; Gorel, A.; Grünbein, M.L.; Hilpert, M.; Hunter, M.; Kloos, M.; Koglin, J.E.; Lane, T.J.; Liang, M.; Mantovanelli, A.; Nass, K.; Kovacs, G.N.; Owada, S.; Roome, C.M.; Schirò, G.; Seaberg, M.; Stricker, M.; Thépaut, M.; Tono, K.; Ueda, K.; Uriarte, L.M.; You, D.; Zala, N.; Domratcheva, T.; Jakobs, S.; Sliwa, M.; Schlichting, I.; Colletier, J.P.; Bourgeois, D.; Weik, M. Rational control of structural off-state heterogeneity in a photoswitchable fluorescent protein provides switching contrast enhancement. *bioRxiv* **2021**, p. 2021.11.05.462999. doi:10.1101/2021.11.05.462999.